



HAL
open science

Thermodynamic uptake of atmospheric CO₂ in the oligotrophic and semiarid São Francisco estuary (NE Brazil)

Gwenaël Abril, Bruno Libardoni, Nilva Brandini, Luiz Cotovicz, Paulo R.P. Medeiros, Geórgenes Cavalcante, Bastiaan Knoppers

► **To cite this version:**

Gwenaël Abril, Bruno Libardoni, Nilva Brandini, Luiz Cotovicz, Paulo R.P. Medeiros, et al.. Thermodynamic uptake of atmospheric CO₂ in the oligotrophic and semiarid São Francisco estuary (NE Brazil). *Marine Chemistry*, 2021, 233, pp.103983. 10.1016/j.marchem.2021.103983 . hal-03375517

HAL Id: hal-03375517

<https://hal.science/hal-03375517>

Submitted on 14 Oct 2021

HAL is a multi-disciplinary open access archive for the deposit and dissemination of scientific research documents, whether they are published or not. The documents may come from teaching and research institutions in France or abroad, or from public or private research centers.

L'archive ouverte pluridisciplinaire **HAL**, est destinée au dépôt et à la diffusion de documents scientifiques de niveau recherche, publiés ou non, émanant des établissements d'enseignement et de recherche français ou étrangers, des laboratoires publics ou privés.

1 **Thermodynamic uptake of atmospheric CO₂ in the oligotrophic and semi-arid São Francisco**
2 **estuary (NE Brazil).**

3

4

5

6 Gwenaël Abril^{1,2,*}, Bruno G. Libardoni², Nilva Brandini², Luiz C. Cotovicz Jr.³, Paulo R. P.
7 Medeiros⁴, Geórgenes H. Cavalcante^{5,6}, and Bastiaan A. Knoppers²

8

9 ¹ Laboratoire de Biologie des Organismes et Ecosystèmes Aquatiques (BOREA), Muséum
10 National d'Histoire Naturelle, FRE 2030, CNRS, MNHN, IRD, SU, UCN, UA, Paris, France.

11 ² Programa de Geoquímica, Universidade Federal Fluminense, Niterói, RJ, Brazil

12 ³ Instituto de Ciências do Mar, Universidade Federal do Ceará, Fortaleza, Ceará, Brazil

13 ⁴ Instituto de Geografia Desenvolvimento e Meio Ambiente, Universidade Federal de Alagoas,
14 Maceio, AL, Brazil

15 ⁵ Instituto de Ciências Atmosféricas, Universidade Federal de Alagoas, Maceio, AL, Brazil

16 ⁶ Department of Biology, Chemistry and Environmental Sciences, College of Arts and
17 Sciences, American University of Sharjah, Sharjah, United Arab Emirates.

18

19

20

21

22 * Corresponding author gwenael.abril@mnhn.fr

23

24 Submitted to Marine Chemistry, revised version

25

26

27

28

29

30 **Abstract**

31 Estuarine carbonate chemistry predicts that thermodynamic equilibration during the mixing of
32 freshwater with seawater will generate a carbon dioxide (CO₂) sink for the case of warm and poorly
33 buffered tropical rivers. The São Francisco River estuary has historically become oligotrophic, after
34 the construction on its watershed of a series of hydroelectric dams, where organic matter and
35 nutrients are retained. During two cruises in late winter (Aug. 2014) and early summer (Nov. 2015),
36 dissolved inorganic carbon (DIC) and total alkalinity (TA) increased linearly with salinity in the main
37 estuarine channel, where the mixing time of water was half a day, and showed a close to
38 conservative behaviour. In the main channel, water partial pressure of CO₂ (pCO₂) recorded at 1-
39 min frequency, followed an asymmetric bell-shaped trend *versus* salinity, close to the curve
40 predicted by thermodynamic conservative mixing of freshwater DIC and TA with seawater DIC and
41 TA. The low (0-3) salinity region was always a source of atmospheric CO₂, where, despite low
42 chlorophyll concentrations, a pCO₂ diurnal change of about 60 ppmv suggested the occurrence of
43 photosynthesis in summer . At salinities above 3, under-saturated pCO₂ values (down to 225 ppmv
44 in winter and neap tides) and invasion of atmospheric CO₂ of 0.38-1.70 mmol m⁻¹ h⁻¹ occurred
45 because of predominating thermodynamics during estuarine mixing. In winter and neap tides,
46 higher river discharge, intense estuarine mixing, lower temperatures and limited tidal pumping
47 resulted in observed pCO₂ different from theoretical conservative pCO₂ by less than 3ppmv at
48 salinities >3. Conversely, in summer and spring tides, recorded pCO₂ values were on average
49 +43±35 ppmv above the conservative mixing curve, when tidal pumping, CO₂ invasion and surface
50 heating were more significant in the mixing zone, but not sufficient to offset the thermodynamic
51 uptake of atmospheric CO₂. By combining carbonate chemistry with estuarine mixing modelling
52 and gas exchange calculations, we estimate that heating contributed to about 15% and gas
53 exchange to about 10% of the positive pCO₂ deviation from conservative mixing during summer.
54 The remaining 75% of the deviation was maximum at ebb tides and within a salinity ranges
55 consistent with the occurrence of tidal pumping from marches and mangrove soils. Indeed, in the
56 mangrove channel, water were supersaturated with pCO₂ values of 976±314ppmv, while in the
57 main channel, highest positive pCO₂ deviations from conservative mixing (up to +100ppmv during
58 several hours) occurred at ebb tides. An important finding was that, in the São Francisco, the

59 thermodynamic and biological processes compete with each other to CO₂ fluxes both at low
60 salinities where evasion and autotrophy occur, and at high salinities where invasion, heterotrophy
61 and tidal pumping occur. Our study suggests that carbonate thermodynamics during mixing is a
62 key process that has been overlooked in estuarine studies, although it can generate important air-
63 water CO₂ exchange and contribute significantly to the carbon budget of estuaries and river
64 plumes.

65

66 **Keywords**

67 Carbonate equilibria, estuarine mixing, tidal pumping, heterotrophy, heating, gas exchange

68

69

70 **1. Introduction**

71 The necessity of reducing uncertainties on global estimates of CO₂ sources and sinks on Earth has
72 promoted research on the carbon cycle in estuarine and coastal ecosystems particularly during the
73 last three decades (Wollast, 1991; Smith and Hollibaugh, 1993; Frankignoulle et al., 1998; Cai,
74 2011; Borges and Abril, 2011; Bauer et al., 2013; Dinauer and Mucci, 2017, Maher et al., 2018).
75 Despite their small surface areas, estuaries have been identified as a hotspot of CO₂ emissions,
76 able to offset a large part of the CO₂ sink on the continental shelves (Chen and Borges, 2009).
77 This conclusion was based on field observations in temperate and boreal regions, where estuaries
78 have been recognized as CO₂ sources and as heterotrophic ecosystems, that is, with a negative
79 net ecosystem production (NEP) (Smith and Hollibaugh, 1993; Borges and Abril, 2011). Upper
80 estuarine regions with generally well-mixed channels are almost always net heterotrophic,
81 supersaturated in CO₂ and a strong source of CO₂ to the atmosphere (Frankignoulle et al., 1998;
82 Borges et al., 2006; Sarma et al., 2012). In contrast, lower estuarine regions with high salinities,
83 including large surfaces of river plumes at sea and coastal embayments, are sites of phytoplankton
84 blooms, and may have a net autotrophic metabolism (positive NEP) at least in the surface layer,
85 and behave as CO₂ sinks, at minima seasonally (Körtzinger, 2003; Borges et al., 2006; Cai et al.,
86 2013; Cotovicz et al., 2015; Lefèvre et al., 2017).

87

88 The global CO₂ emissions from estuaries suffer from large uncertainties due to spatial and
89 temporal heterogeneity (Chen and Borges, 2009). In most studies, the relationship between NEP
90 and CO₂ fluxes could not be established quantitatively because many processes other than
91 community respiration and primary production can alter the partial pressure of CO₂ ($p\text{CO}_2$) and the
92 direction and intensity of the air-sea CO₂ flux in estuaries (Borges, 2005). For instance, in
93 eutrophic estuaries, nitrification can titrate TA to CO₂, contrarily to carbonate dissolution that can
94 consume CO₂ and generate TA (Frankignoulle et al., 1996; Abril and Frankignoulle, 2001; Abril et
95 al., 2003; Cotovicz et al., 2021). Some dissolved CO₂ transported laterally from freshwaters or tidal
96 marshes and mangroves is ventilated in river-dominated and/or macrotidal estuaries (Abril et al.,
97 2000; Neubauer and Anderson, 2003; Borges et al., 2003; 2006; Cai, 2011). In general, advection
98 of surface or sub-surface waters enriched in DIC, and/or biodegradable organic carbon (OC), as

99 well as the presence of vegetation at the land-water interface, complicates the calculation of NEP
100 and its relationship with CO₂ fluxes (Borges, 2005; Cai, 2011; Borges and Abril, 2011; Santos et
101 al., 2018; Maher et al., 2018).

102
103 In estuaries, water pCO₂ is also strongly modified by the displacement of the acid-base equilibria of
104 the carbonate system during the mixing of freshwater with seawater. As a consequence, the
105 concentrations of bicarbonate (HCO₃⁻) and carbonate (CO₃²⁻) ions, as well as pCO₂ in a mixture of
106 two waters with different salinities and temperatures, are very different from the arithmetic mean of
107 these parameters in the two waters. In their pioneer theoretical work, Whitfield and Turner (1986)
108 applied newly published carbonate dissociation and gas solubility constants to calculate the
109 theoretical distribution of pCO₂ along the salinity gradient induced by the conservative mixing of
110 DIC and TA from the freshwater and marine end-members. These authors showed that “*the mixing*
111 *of river water and sea water [...] tends to produce significant disequilibrium between the estuary*
112 *and the atmosphere which may manifest itself as a deficit or as an excess of carbon dioxide,*
113 *depending on the pH and alkalinity of the river water.*” However, in recent years, studies rarely
114 consider in detail carbonate thermodynamic during mixing as a potential driver of estuarine CO₂
115 fluxes, although it can generate some atmospheric CO₂ release or uptake additional to NEP (Cai et
116 al., 2013; Lefèvre et al., 2017; Delaigue et al., 2020; Cotovicz et al., 2020). Most studies have
117 focused on the correlation between biological components of NEP and CO₂ fluxes (Borges and
118 Abril 2011), and lateral C fluxes induced by tidal inundation and pumping (Cai, 2011; Maher et al.,
119 2013; 2018). In the Amazon plume, a large part of the CO₂ sink at salinities higher than 17 could
120 be attributed to thermodynamics, but unfortunately no pCO₂ field data are available at salinities
121 lower than 17 (Körtzinger, 2003; Cai et al., 2013; Lefèvre et al., 2017). Recently, Cotovicz et al.
122 (2020) reported a CO₂ sink in the estuarine delta of the Paraíba do Sul River induced by a
123 combination of carbonate thermodynamics, ecosystem metabolism and temperature effects.
124 Although it is essential in the open ocean, the role of surface water heating or cooling on CO₂
125 fluxes is poorly documented in estuarine waters. In tropical and sub-tropical coastal systems,
126 surface heating and evaporation can have a large impact on CO₂ water-air fluxes (Yao and Hu
127 2017; Cotovicz et al., 2020; Yao et al. 2020).

128 In the present study, we report high resolution data of the carbonate system in a tropical,
129 oligotrophic estuary with short mixing time, where thermodynamics alone explains a large part of
130 the well-defined $p\text{CO}_2$ distribution. Owing to warm temperatures and low TA at the river end-
131 member, the São Francisco estuary presents conditions that theoretically generate CO_2 invasion
132 during estuarine mixing, even when supersaturation prevails in the river, a case similar to large
133 tropical rivers such as the Amazon and the Congo (Cai et al., 2013). The oligotrophic character of
134 the estuary and the short mixing time make chemical and physical processes predominate over
135 biological processes. The estuary is also connected to a small mangrove forest that may export
136 dissolved carbon to waters (Maher et al., 2013), and is subjected to important heating owing to the
137 semi-arid evaporative conditions in summer.

138

139 **2. Material and methods**

140 2.1. Study area

141 The São Francisco River (Fig. 1) drains an area of 634 000 km² in Brazil that includes Pleistocene-
142 Holocene plains (Dominguez, 1996). Precambrian rocks of the Brazilian shield dominate the
143 geology of the basin, and the climate varies from tropical humid in the upper and lower regions, to
144 semiarid in the middle region (Bernardes, 1951). The River course has been progressively
145 intensively modified between the 50's and the 90's by the construction of five hydroelectric
146 reservoirs, which had strong impacts on the estuary. Decreased precipitations combined to an
147 increased evaporation due to the presence of dams on the watershed have reduced the average
148 annual freshwater discharge from about 2,895 m³s⁻¹ (1961-1990) to about 1,800 m³s⁻¹ (after Xingó
149 Dam) in 1995 and to less than 1000m³s⁻¹ during the last decade (Bernardes et al., 2012;
150 Cavalcante et al., 2017; de Jong et al., 2018). Floods that strongly influenced the estuarine
151 morphology were suppressed, and most of the riverine suspended sediments, nitrogen,
152 phosphorus and silica were retained in reservoirs, turning the estuary oligotrophic, with chlorophyll
153 concentrations lower than 3 µg L⁻¹ in more than 95% of the samples from recent years (Medeiros
154 et al., 2011; 2018; Melo et al., 2020; Melo-Magalhães et al. 2015). Today, the estuarine
155 morphology consists in a stratified, salt-wedge type, main channel, separated from the sea by a
156 shallow area of submerged dynamic sandy banks, and a secondary channel in the South,

157 surrounded by mangroves that have been partly deforested for shrimp farming. Water depth in the
158 main channel in on average 3m, with a maximum of 12m and very shallow depth at the mouth,
159 where sandy banks separate the estuary from the shelf. Strong saline stratification occurs in the
160 main channel and tidal movements generate large variations in surface water salinity and
161 extension of the plume on the shelf (Cavalcantes et al. 2020). Residence time of freshwater in the
162 inner estuary with the surface area of 19km² is about half a day (Cavalcante et al. 2017). About 5%
163 of the freshwater transits through the secondary channel and ends-up in a shallow coastal lagoon
164 parallel to the coast and connected to the sea at high tide through several narrow canals (Fig.1).

165

166 2.2. Fieldwork, chemical analyses and calculations

167 Sampling occurred in late winter the 5-8th of August 2014 and in early summer the 11-14th of
168 November 2015, when river discharges were, respectively, 1220 and 950m³s⁻¹, and the tidal
169 ranges were 1.2 m (end of neap tides) and 1.8 m (spring tides). Detailed descriptions of all
170 methods for *in-situ* measurements, discrete water sampling and preservation can be found in
171 Cotovicz et al., (2015) and Cotovicz et al., (2020). Field work consisted in measurement every
172 minute of *p*CO₂ salinity and temperature, and sampling of surface water from freshwater to coastal
173 waters (Salinity >30) in both channels. Discrete samples were taken along the salinity gradient in
174 the two channels at approximately two-salinity intervals, except in the salinity range 10-25, where
175 changes were too abrupt to allow sampling at regular salinity intervals. Three end-members could
176 be sampled (Fig. 1): the centre of the river main channel, the mouth of the main channel (salinity ~
177 30), and a shallow coastal lagoon at the outlet of the secondary mangrove channel (Salinity 30-
178 34). The 11-12th of Nov. 2015, measurements were also performed during 25h at an anchored
179 station in the main channel, where salinity varied from 1.2 at low tide to 32.2 at high tide.

180 Continuous measurements were performed during the vessel's travels or at the anchored station,
181 by pumping surface water at 8L min⁻¹ to a 1L vial containing the sondes and a marble-type
182 equilibrator (Frankignoulle et al., 2001). The marble equilibrator consisted in an acrylic tube filled
183 with glass marbles where water flows from the top, and a closed air circuit with a flux of about (1 L
184 min⁻¹), flowing in the opposite direction from the bottom to the top. The air is dried with drierite and
185 pumped to a non-dispersive infrared (NDIR) gas analyser (LICOR© LI- 820). Before and after each

186 sampling campaigns, the NDIR was calibrated using gas standards with air $p\text{CO}_2$ values of 410,
187 1007 and 5035 ppmv (White Martins Certified Material, RJ, Brazil). Fresh soda lime was used to
188 set the zero and the standard at 1007 ppmv to set the span. The air standards of 410 and 5035
189 ppmv were used to verify the linearity of the response. The accuracy of the $p\text{CO}_2$ measurements is
190 estimated at ± 5 ppmv. Water was continuously overflowing from the 1L vial that hosted a YSI®
191 Professional Plus multiparameter sonde that measured Temperature, salinity and dissolved
192 oxygen (DO) , and a WTW® 3310 pH meter equipped with a Sentix 41 electrode. The pH meter
193 was calibrated daily with a three-point standard (pH 4.01, pH 7.00 and pH 10.01) according to the
194 National Institute of Standards and Technology (NIST). The precision of the pH measurements
195 estimated after seven verifications against standards was about 0.01 NBS units. The salinity probe
196 was calibrated before the cruise with IAPSO standard seawater and deionized water. DO was
197 measured with a polarographic electrode calibrated every morning at 100% saturation in vapor-
198 saturated air. Temperature values measured with the YSI® salinity probe differed from those
199 measured with the WTW® pH-meter by less than 0.1°C. For continuous measurement performed
200 during sailing, the ship speed was adapted according to the salinity changes and varied between
201 Total alkalinity (TA) was titrated on the discrete samples with certified 0.1N HCl on duplicate 50 mL
202 0.7 μm -filtered samples, using the Gran function to determine the equivalent point.

203

204 The concentration of DIC carbonate system was calculated in the discrete samples from the
205 measured $p\text{CO}_2$ and TA, with the CO2sys program (Pierrot et al. 2006) using the CO_2 solubility
206 from Weiss (1974) and the dissociation constants of Mehrbach et al. (1973), refitted by Dickson
207 and Millero (1987). One important precaution for the use of this set of constants is to check for the
208 absence of organic alkalinity at significant concentrations compared to carbonate alkalinity,
209 particularly in the freshwaters (Cai et al., 1998; Hunt et al., 2011; Abril et al., 2015). In order to
210 identify an eventual bias induced by the interference of organic alkalinity in the calculations of DIC,
211 we used our pH measurements concomitant to TA measurements in order to calculate $p\text{CO}_2$
212 (pH/TA) in our discrete samples. The $p\text{CO}_2$ values calculated from pH and TA and those measured
213 directly with the equilibrator were fairly consistent ($< \pm 10\%$), except in a freshwater small tributary
214 on the left edge of the São Francisco River (North of Fig.1 and Fig. S1) that drains a small wetland,

215 and where the calculated $p\text{CO}_2$ (pH/TA) was more than 4 times higher than the measured $p\text{CO}_2$
216 (Cotovicz et al. 2016). However, this tributary does not contribute significantly to the river
217 discharge, as confirmed by our conductivity monitoring at the confluence, and organic alkalinity
218 does not appear to significantly interfere in the calculation of the carbonate system in the São
219 Francisco main channel and mangrove channel.

220

221 In this work, we analyse and compare the distribution along the salinity gradient of four types of
222 $p\text{CO}_2$: the $p\text{CO}_2$ observed *in situ*, noted O- $p\text{CO}_2$, the $p\text{CO}_2$ resulting from conservative mixing of
223 river water with seawater, noted C- $p\text{CO}_2$, the $p\text{CO}_2$ normalized to temperature, noted T- $p\text{CO}_2$, and
224 the $p\text{CO}_2$ resulting from conservative after being corrected for gas exchange, noted Ex- $p\text{CO}_2$. For
225 each campaign we established the equations of the conservative mixing lines for TA, DIC and
226 temperature as a function of salinity, using the values at the two end-members: the reference
227 freshwater station at the centre of the main channel upstream and the most saline sample at the
228 mouth downstream (Fig. 1). Then the C- $p\text{CO}_2$ thermodynamic conservative mixing curves were
229 calculated for each salinity value where continuous measurements were performed, using the
230 calculated conservative (linear) values of temperature, TA and DIC between the two end-members
231 in the main channel. We evaluated the impact of water heating on $p\text{CO}_2$ in the main channel and in
232 the secondary channel passing through the mangrove, by normalizing the O- $p\text{CO}_2$ observed at a
233 given salinity at the temperature corresponding to the linear interpolation of the temperatures in the
234 freshwater and marine end-members. To that end, we calculated for each salinity point
235 measurement, a temperature-normalized T- $p\text{CO}_2$ from the measured $p\text{CO}_2$ the conservative TA
236 mixing line, and the lowest temperatures observed at each end-member, generally at night and
237 early morning. In winter and neap tides (Aug. 2014), two distinct temperature marine end-members
238 should be considered: one at the mouth of the main channel and another one in the coastal lagoon
239 at the mouth of the mangrove channel (Fig. 1). In contrast, a single set of freshwater and seawater
240 temperature end-members could be used during summer and spring tides (Nov. 2015) when
241 consistent cooler night-time waters were observed in both marine end-members (see results
242 section).

243

244 The evasion or invasion of CO₂ at the water-air interface was calculated according to:

$$245 \quad FCO_2 = k\alpha\Delta pCO_2 \quad \text{Eq.1}$$

246 where FCO₂ is the water-air CO₂ flux (mol m⁻² h⁻¹), k is the gas transfer velocity (m h⁻¹), α is the
247 solubility coefficient (mol m⁻³ atm⁻¹) and ΔpCO₂ is the difference between water and air pCO₂ (in
248 atm). Atmospheric pCO₂ was measured every morning and evening by pumping with the NDIR gas
249 analyser and daily average values were used for the flux calculation. To calculate k, we apply three
250 equations as a function of the concomitant wind speed at 10 meters (U10) recorded at a station
251 located 4km landward (Fig.1). The equations of Wanninkhof 1992 (noted W92) and Raymond and
252 Cole (2001) (noted RC01) provide the gas transfer velocity as a function of U10, and the equation
253 of Abril et al. (2009) (noted A09) as a function of U10, estuarine surface area and water current
254 velocity. In the A09 model, we used a surface area of 19 km², and an average water current of 0.4
255 m s⁻¹ as representative for the São Francisco main channel (Cavalcante et al., 2017). For all
256 calculations, pCO₂ and wind speed data were selected in order to calculate FCO₂ in winter and
257 summer at daytime and in summer at night-time.

258

259 To complete our study, we corrected the theoretical C-pCO₂ conservative mixing curves for the air-
260 water CO₂ exchange, building Ex-pCO₂ curves. We applied an iterative calculation every salinity
261 unit from 0 to 34, of the loss or gain of DIC as CO₂ evasion or invasion during the mixing of water
262 at salinity s with seawater to reach the value of salinity s+1.

$$263 \quad DIC_{gain}(s) = -FCO_2(s).RT.H^{-1} \quad \text{Eq.2}$$

264 where FCO₂(s) is the flux (mol m⁻² h⁻¹), RT is the residence time (h) and H is the water depth (m).

265 FCO₂(s) is calculated with Eq.1 and the C-pCO₂ value at salinity s, deduced from the mixing of
266 DIC(s) with DIC(34) and TA(s) with TA(34). Then, the new corrected DIC concentration at s+1,
267 DIC(s+1), is obtained by adding the DICgain(s) to the DIC(s):

$$268 \quad \text{Corrected DIC}(s+1) = DIC(s+1) + DIC_{gain}(s) \quad \text{Eq.3}$$

269 At that step, we recalculate a corrected C-pCO₂(s+1) from new mixing between corrected DIC(s+1)
270 and DIC(34), and TA(s+1) and TA(34). The next iteration consisted in calculating the FCO₂(s+1)
271 from the corrected C-pCO₂(s+1) and the DICgain(s+2) using Eq.1. The model was set-up in the

272 CO2sys spreadsheet (Pierrot et al. 2006), each line representing a salinity increment of one unit,
273 from zero to 34, with the possibility to choose the gas transfer equation, the U10, RT and H.
274 Incrementation of the model allowed the building of thermodynamic Ex- $p\text{CO}_2$ mixing curves
275 corrected from gas exchange according to various combinations of these parameters. We used an
276 RT/H ratio of 0.17 day m^{-1} which corresponds to a short RT value in the São Francisco estuary of
277 0.5 day as estimated from the discharge during the cruise, a mean H of 3m and an estuarine
278 surface of 19km^2 . In order to simulate conditions closer to the ones occurring in large river plumes,
279 we also tested the influence of increasing RT/H to 0.33 and 0.5 day m^{-1} , and we applied three
280 different wind speeds of 0.5, 3 and 7 m s^{-1} , as representative of estuarine and shelf meteorological
281 conditions. In addition, we assumed that the residence time was uniformly distributed along the
282 salinity gradient, although there might be some exceptions as for instance longer residence times
283 (several tidal cycles) in the low salinity range.

284

285 **3. Results**

286 DIC and TA increased linearly with salinity in the main channel, respectively from 553 ± 40 and
287 $539\pm 27 \mu\text{mol kg}^{-1}$ in the river end-member to 1719 ± 127 and $1975\pm 146 \mu\text{mol kg}^{-1}$ at the mouth with
288 salinity >30 (Fig. 2). Some significant positive anomalies of both parameters were observed at high
289 salinity stations in the mangrove channel (Fig. 2). During both cruises, O- $p\text{CO}_2$ was highly variable
290 in the freshwater with some lateral heterogeneity between the different channels, and was above
291 the atmospheric $p\text{CO}_2$ at the centre of the main channel, with a value of $\sim 700\text{ppmv}$ (Fig.3A&B).
292 Downstream in the main channel, O- $p\text{CO}_2$ sharply decreased below 400ppmv at salinity 3, and
293 followed an asymmetric bell-shaped curve along the salinity gradient. In winter, O- $p\text{CO}_2$ distribution
294 in the main channel was almost perfectly predicted by thermodynamics during mixing with average
295 difference between O- $p\text{CO}_2$ and C- $p\text{CO}_2$ in the 3-30 salinity range being $3\pm 13 \text{ ppmv}$ (Table 1), that
296 is, within the error of $p\text{CO}_2$ measurements and mixing model calculations. In summer, however, O-
297 $p\text{CO}_2$ in the main channel was on average $43\pm 35 \text{ ppmv}$ above the theoretical mixing curve of C-
298 $p\text{CO}_2$ along the 3-30 salinity range at night-time and daytime. Measured O- $p\text{CO}_2$ included under-
299 saturated values and invasion of atmospheric CO_2 at salinities above 3 during both cruises
300 (Fig.3A&B). The most marine waters with salinities >30 were under-saturated in Aug. 2014 (O-

301 $p\text{CO}_2$: 332 ppmv) and almost at equilibrium (O - $p\text{CO}_2$: 403 ± 18 ppmv) in Nov. 2015 (Fig. 3E&F). In
302 the mangrove channel, O - $p\text{CO}_2$ was higher and more variable than in the main channel: between
303 298 and 975 ppmv (mean 512 ppmv) in winter and between 307 and 2007 ppmv (mean 976 ppmv)
304 in summer (Fig. 3A&B). Several O - $p\text{CO}_2$ peaks occurred in the mangrove channel and the
305 adjacent coastal lagoon, at intermediate and high salinities and variations also occurred according
306 to the tidal phase, with higher values in Nov. 2015 corresponding to low tide at spring tide period. A
307 maximum of 2000 ppmv was recorded in the coastal lagoon at the outlet of the mangrove channel
308 during the afternoon at low tide (Fig. 3B). During the two cruises DO remained between 99% and
309 101% saturation throughout most of the salinity gradient in the main channel (Fig. S2). At both
310 seasons, significant DO undersaturation occurred in the river at low salinities and in the mangrove
311 channel, with lower minimum values in Nov. 2015 compared to Aug. 2014. In Nov. 2015, slight DO
312 oversaturation (max 103%) was observed in the main channel at salinities around 3 and above 31
313 (Fig. S2).

314
315 Water temperatures were lower in Aug. 2014 than in Nov. 2015 (Fig. 3C,D). During winter and
316 neap tide (Aug. 2014), temperature remained constant in the main channel, and about 1°C above
317 the conservative mixing line in the mangrove channel, showing that water heating occurred (Fig.
318 3C). In Aug. 2014, O - $p\text{CO}_2$ was higher than the T - $p\text{CO}_2$ by 5-20ppmv in the mangrove channel,
319 but less than 2ppmv in the main channel (Fig. 3E). In Nov. 2015, when measurements were also
320 performed at night, surface heating was evident from night-time to daytime, as well as, within the
321 mixing zone in comparison with the two end-members. The entire salinity gradient in both channels
322 was more than 1°C cooler at night and early morning (before 9h) than at daytime and dusk (Fig.
323 3D), which resulted in O - $p\text{CO}_2$ higher than the T - $p\text{CO}_2$ by 10-15ppmv (Fig. 3F). A peak
324 temperature of 29.8°C occurred in Nov. 2015 during the afternoon in the shallow lagoon at the
325 outlet of the mangrove channel at low tide, which corresponded to a O - $p\text{CO}_2$ 120ppmv higher than
326 T - $p\text{CO}_2$, when the O - $p\text{CO}_2$ reached 2000 ppmv (Fig. 3F).

327
328 During the 25h cycle at the anchored station in the main channel the 11th and 12th of Nov. 2015,
329 salinity varied between 1.2 and 32.2, and water $p\text{CO}_2$ varied between 238 ppmv at intermediate

330 salinities and 476ppmv at low salinity. The record at one minute frequency revealed a remarkable
331 parallelism between O- $p\text{CO}_2$ and C- $p\text{CO}_2$ calculated from the mixing of the two end-members and
332 the salinity value. However, O- $p\text{CO}_2$ was on average $+43\pm 35$ ppmv above the conservative mixing
333 curve o C- $p\text{CO}_2$ (Fig. 4). Maximum deviations of O- $p\text{CO}_2$ from C- $p\text{CO}_2$ occurred during the ebb
334 tides, both at sunset and night (hours 1.5 to 4.2: 52 ± 19 ppmv) and at sunrise and early morning
335 (hours 13.5 to 17.5: 92 ± 30 ppmv). In addition, at low tide when salinities were below 3, O- $p\text{CO}_2$
336 values were close to the C- $p\text{CO}_2$ at daytime (hours 19-21.5), but were ~ 60 ppmv higher than C-
337 $p\text{CO}_2$ at night-time (hours 7-10) indicating diurnal variations in this low salinity range (Fig. 3).
338 Finally, throughout the 25h cycle, some heating effect on $p\text{CO}_2$ was detected during the afternoon
339 at high tide and high salinity (hours 1 and 25) and at low tide and low salinity (hour 20), when O-
340 $p\text{CO}_2$ was at maximum $+25$ ppmv higher than T- $p\text{CO}_2$ (Fig. 4B).

341

342 Wind speed was low during the cruises, always below 3.5 m s^{-1} , on average between 1.1 m s^{-1} in
343 Nov. 2015 and 2.2 m s^{-1} in April at day time, and 0.5 m s^{-1} at night-time (Table 1). In the main
344 channel, FCO_2 fluxes varied between 0.01 and $0.79 \text{ mmol m}^{-2} \text{ h}^{-1}$ (positive fluxes for CO_2 evasion)
345 in the 0-3 salinity range and between -0.04 and $-1.68 \text{ mmol m}^{-2} \text{ h}^{-2}$ in the 3-30 salinity range. In the
346 mangrove channel, calculated FCO_2 varied between 1.23 and $10.72 \text{ mmol m}^{-2} \text{ h}^{-1}$. For the
347 observed wind speed range, calculated FCO_2 strongly depended on the choice of the k_{600}
348 parameterization, the W92 equation giving lower fluxes than the RC01 and A09 equations (Table
349 1).

350

351 Ex- $p\text{CO}_2$, the theoretical thermodynamic $p\text{CO}_2$ mixing curves corrected for gas exchange, were
352 below the standard conservative curve between salinities 0 and 3-5, where CO_2 evasion occurs,
353 and above the curve between salinities 3-5 and 34, where invasion of atmospheric CO_2 occurs
354 (Fig. 5). Computed deviation from conservative mixing, i.e. Ex- $p\text{CO}_2$ minus C- $p\text{CO}_2$ strongly
355 depended on the selected parameters, the gas transfer parametrization, the U10 and the
356 residence time / depth ratio. These deviations varied from -0.3 to -167 ppmv (average -29 ppmv) in
357 the 0-3 salinity range and from -8 to $+76$ ppmv (average $+16$ ppmv) in the 3-30 salinity range.
358 Applying a residence time in the São Francisco estuary of 0.5 days during the cruises, an average

359 water depth of 3m and the U10 values of 0.5 and 3 m s⁻¹ as representative for the conditions
360 during the cruise, gives Ex-*p*CO₂ - C-*p*CO₂ values of -12±9ppmv in the 0-3 salinity range and
361 4±3ppmv in the 3-30 salinity range (Table 1).

362

363

364 **4. Discussion**

365 4.1. Predominance of thermodynamics

366 In the main channel, the *p*CO₂ measurements (O-*p*CO₂) and the thermodynamic estuarine
367 conservative mixing model (C-*p*CO₂) follow the same asymmetric bell-shape curve, with a steep
368 decrease from salinity zero to 3, and undersaturation of surface waters all along the 3-30 salinity
369 gradient (Fig. 3). To date, such well-defined *p*CO₂ curve, with high resolution measured values
370 very consistent with the theoretical conservative mixing curve, have been reported in the Amazon
371 plume only for salinities higher than 17, and in the tropical Paraíba do Sul along the entire salinity
372 gradient, with continuous *p*CO₂ measurements (Cotovicz et al., 2020). In the mesotrophic Paraíba
373 do Sul River Estuary, autotrophic and heterotrophic activities had strong influences on the *p*CO₂
374 distribution along the salinity gradient at low river discharge, but not at high discharge and shorter
375 residence time, when the *p*CO₂ versus salinity plot followed the theoretical curve (Cotovicz et al.
376 2020). Because of the oligotrophic character of the São Francisco estuary (Medeiros et al. 2011;
377 2018) and the short residence time of water in the mixing zone (half a day), thermodynamics
378 predominates over biological processes in controlling estuarine *p*CO₂ distribution along the
379 estuarine gradient. Some theoretical works have described how thermodynamics during estuarine
380 mixing can generate positive or negative air-water CO₂ fluxes depending on the DIC and TA
381 concentrations in the river end-member, the concentrations in the marine end-member being
382 considered as constant in comparison (Whitfield and Turner, 1986; Cai et al., 2013; Delaigue et al.
383 2020). In the case of the São Francisco with a low TA river end-member (around 500 μmol kg⁻¹),
384 and warm waters (above 25°C), thermodynamics during mixing turns the estuary into a sink of
385 atmospheric CO₂ (Whitfield and Turner, 1986); this is also the same for the Amazon (TA of 450
386 μmol kg⁻¹) and the Congo (300 μmol kg⁻¹) but not the Mississippi (>2000 μmol kg⁻¹), where
387 carbonate thermodynamics generates a CO₂ source and where the observed CO₂ invasion is

388 biological as revealed by nitrate uptake (Cai et al., 2013). Although the conditions found in the
389 largest world rivers potentially generate a CO₂ sink in the coastal zone, very few *in-situ* pCO₂ data
390 cover a complete estuarine salinity gradient consistent with the pCO₂ theoretical mixing curve (Cai
391 et al. 2013; Lefèvre et al. 2017; Cotovicz et al. 2020). In winter in the São Francisco estuary, the
392 average difference between O-pCO₂ and C-pCO₂ was only 3±13 ppmv along the 3-30 salinity
393 range in the main channel and thermodynamics was apparently the unique driver of the carbonate
394 system, creating a permanent CO₂ influx in this salinity range. In summer, the average difference
395 between O-pCO₂ and C-pCO₂ at salinities > 3 was +49±39 ppmv at daytime and +36±22 at night-
396 time (Table 1), but O-pCO₂ always remained below the atmospheric value of 400 ppmv at salinities
397 above 3, and thermodynamic uptake of atmospheric CO₂ was predominant.

398

399 Our continuous measurements in the São Francisco also allow an interpretation of these O-pCO₂
400 deviations from C-pCO₂ as the result of other internal CO₂ sources and sinks. First, estuarine NEP
401 and lateral transport from river and intertidal areas can be a source of CO₂ (Abril and Borges,
402 2011; Bauer et al., 2013). Second, C-pCO₂ simulations were based on the conservative mixing of
403 temperature at daytime at the two end-members, although heating and cooling of water is a
404 common feature in this semi-arid region, and can potentially change pCO₂ at daily and tidal time
405 scales, particularly in shallow regions of the estuary such as the lagoon. Third, while air-water
406 exchange of CO₂ is much slower than acid-base equilibration of DIC species, evasion and invasion
407 of CO₂ occur during estuarine mixing, potentially altering the thermodynamic pCO₂ curve. All these
408 processes can generate pCO₂ changes of few tens of ppmv that can add up to the values of pCO₂
409 deviations from the mixing curves in summer (Cotovicz et al., 2020). However, when interpreting
410 these deviations, we must also keep in mind that the shape of the modelled C-pCO₂ curve
411 depends on the choice of the freshwater end-member, which was difficult to define because of
412 lateral heterogeneity. For example, we calculated that using a freshwater end-member with 5µmol
413 kg⁻¹ higher TA (or DIC) (a change within the range of analytical precision for these parameters),
414 generates mixing pCO₂ values 10 ppmv lower (or 9 ppmv higher) at salinity 10. In the case of our
415 study, we choose to use the TA and pCO₂ values at the central and deepest station upstream all
416 the small islands (Fig. 1), where most freshwater flows and with little tidal influence, and not an

417 average of all measurements at the lowest salinity (<0.1) region. Owing to the significant
418 heterogeneity in the different canals, we cannot totally exclude lateral input of freshwater from
419 small tributaries in this region that alter the DIC concentrations in the end-member and the
420 modelled mixing $p\text{CO}_2$ curve.

421

422 4.2. Biological CO_2 sources and sinks

423 The diurnal O- $p\text{CO}_2$ change at low salinity (Fig. 4) reveals some photosynthetic activity in this
424 region, despite the chlorophyll concentration around $3 \mu\text{g L}^{-1}$ (unpublished data). During our
425 measurements (Fig. 4), the respiration of this plankton apparently generated a deviation of +60
426 ppmv above the conservative mixing at night-time and early morning (hours 7-9), compared to the
427 afternoon when phytoplankton absorbed CO_2 (hours 21-23). Concomitant change in DO could be
428 detected, although the DO values remained very close to 100% at night time and daytime in the
429 whole salinity range. We calculated that, for the conditions of Nov. 2015, the diurnal change of 60
430 ppmv of O- $p\text{CO}_2$ at salinity 3 corresponds to a change in DIC of $5 \mu\text{mol kg}^{-1}$. If we assume a
431 photosynthetic/respiratory quotient of 1, the equivalent diurnal change in DO in these oligotrophic
432 waters would be about 2%sat. In fact, in Nov. 2015, the DO concentration at salinity 3 was 100%
433 at night time and 103% at daytime (Fig. S2), but these differences remained close to the error in
434 DO measurements. Consequently, $p\text{CO}_2$ monitoring was much more powerful than O_2 monitoring
435 to detect photosynthetic activity in the oligotrophic São Francisco estuary. It is well known that
436 freshwater phytoplankton can still be active in estuaries at low salinities, but generally not at higher
437 salinities in the mixing zone, where they die due to saline stress (Lancelot and Muylaert, 2012).
438 This is probably the case in the São Francisco estuary, where, despite the general low biomass,
439 freshwater phytoplankton potentially fuels heterotrophy downstream in the main channel. However,
440 the residence time of half a day is probably too short to allow the well establishment of an active
441 heterotrophic community (Crump et al., 2004). Benthic heterotrophy is probably limited in the
442 sandy sediments of the São Francisco estuary where strong hydrodynamics limits the deposition of
443 fine organic biodegradable material (Medeiros et al. 2007). Along the salinity gradient, the
444 deviation of O- $p\text{CO}_2$ from C- $p\text{CO}_2$ was spatially and temporally linked to tidal advection from
445 mangroves and other brackish marshes. Many authors have reported high CO_2 degassing fluxes

446 from mangrove surrounding waters (Borges et al., 2003; Maher et al., 2013; Santos et al., 2018;
447 Cotovicz et al., 2020). High water $p\text{CO}_2$ come from the tidal pumping of mangrove-saturated soil
448 CO_2 (Maher et al., 2013; Santos et al., 2018), and from the respiration of mangrove-derived
449 organic matter in creek waters and sediments (Bouillon et al., 2003; Borges and Abril, 2011). In the
450 mangrove's soils, a large part of the metabolism is sulphate reduction that stoichiometrically
451 produces the same amount of TA than CO_2 (Borges et al., 2003). This explains the positive TA
452 (and associated DIC) anomalies observed at high salinities in the mangrove channel of the São
453 Francisco Estuary (Fig. 2). Although water $\text{O-}p\text{CO}_2$ was similar during both campaigns in the main
454 channel, in the secondary channel, $p\text{CO}_2$ values were much higher, particularly in Nov. 2015
455 compared to Aug. 2014. This can be attributed to the spring tide conditions during sampling in
456 2015, enhancing the tidal pumping (Maher et al., 2013; Santos et al., 2018). During the 25h cycle
457 in the main channel at spring tide in 2015 (Fig.4), the highest (>100 ppmv) and longest positive
458 deviations of $\text{O-}p\text{CO}_2$ from $\text{C-}p\text{CO}_2$ occurred during the ebb tides, particularly at late night and
459 early morning (hours 14-17) which reveals an export from the mangrove waters to the main
460 channel that affects the 5-8 salinity range (Fig.3B). The monitoring point during 25h was located at
461 less than two km from confluence between the main channel and the mangrove channel, and also
462 close to brackish tidal marshes (Fig.1) that could contribute, together with mangroves to the $p\text{CO}_2$
463 peaks at high and ebb tide. In addition, the short residence time of waters in the estuary suggests
464 that heterotrophs would spend little time in the main channel and would be exposed to strong
465 salinity stress to generate significant respiratory CO_2 , which is apparently coming in majority from
466 tidal pumping.

467

468 4.3. Impact of heating

469 Semi-arid coastal ecosystems are environments where heating and evaporation can have a strong
470 influence on the water chemistry and where very few studies document the behaviour of the
471 carbonate system (Leopold et al., 2016; Yao and Hu, 2018; Yao et al., 2020). Heating of water will
472 first increase the $p\text{CO}_2$ and favour outgassing (Takahashi et al., 2002). If evaporation is intense
473 and leads to hypersaline conditions, consumption of TA and release of CO_2 due to carbonate
474 precipitation can occur (Murgulet et al., 2018; Yao et al., 2020). In the São Francisco estuary,

475 higher temperature relative to the mixing of the two end-members was most pronounced during
476 summer and in the mangrove secondary channel (Fig. 3C,D). In summer, despite the short
477 residence time of waters, the temperature increased in both channels by more than 1°C during
478 daytime compared to night-time (Fig. 3D), which corresponds to a theoretical $p\text{CO}_2$ increase
479 (difference between O- $p\text{CO}_2$ and T- $p\text{CO}_2$) of ~15ppmv (Fig. 3F). In the main channel, the 25h
480 cycle (Fig.4) reveals that heating at daytime has a significant impact on $p\text{CO}_2$ at both low tide (hour
481 21) and high tide (hours 1 and 25). In Nov. 2015 at salinities > 3, averaged observed $p\text{CO}_2$ in the
482 main channel in summer were 33ppmv higher during daytime than during night-time, and the
483 thermal effect contributed to 25% of the deviation of $p\text{CO}_2$ above the conservative curve at daytime
484 and 10% at night, when estuarine waters still remained warmer than predicted from the mixing of
485 the end-members (Table 1). At salinities < 3, the thermal effect was partially offset by biological
486 productivity and the O- $p\text{CO}_2$ were similar at night-time and daytime. However, the daytime data
487 included salinities below 1.4 with higher O- $p\text{CO}_2$, whereas night-time data did not (Table 1). In the
488 secondary channel, the maximal thermal effect occurred at salinity ~28 in the coastal lagoon in the
489 afternoon at low tide, with an increase in temperature of ~3°C concomitant with a maximum $p\text{CO}_2$
490 of ~2000ppmv (Fig.3C,F). The thermal effect at this site (Fig.3F) contributed to 15% of the
491 deviation of $p\text{CO}_2$ above the conservative curve at maximum (Fig.3B), and this $p\text{CO}_2$ peak is
492 attributed to the maximum pumping of mangrove-derived CO_2 at low tide. Although water depth
493 was less than half a meter and temperature reached 29.8°C, we found no evidence of carbonate
494 precipitation during this event as those reported in other semi-arid coastal lagoons (Yao et al.,
495 2020). Indeed, the salinity was only 28 during the $p\text{CO}_2$ peak and increased only when the tide
496 started to enter the system through the small canals (Fig.1); no significant TA consumption could
497 confirm carbonate precipitation, TA was above the mixing line in this region, as a result of tidal
498 pumping of DIC from predominant sulphate reduction and other anaerobic processes in the
499 mangrove soils (Borges et al., 2003; Santos et al., 2018).

500

501 4.4. Impact of gas exchange

502 The fact that thermodynamic mixing in the main channel generates undersaturated $p\text{CO}_2$
503 conditions with respect to the atmosphere implies that uptake of atmospheric CO_2 will occur at

504 salinities > 3. Consequently, the hypothesis of conservative DIC mixing on which the
505 thermodynamic $p\text{CO}_2$ curve relies will become invalid, whereas that of conservative TA will remain
506 valid. If we consider the average and standard deviation air-water CO_2 fluxes calculated with the
507 conservative $p\text{CO}_2$ mixing curve and the three gas exchange equations (Table 1), then
508 thermodynamic during mixing in the main channel emits $+2.5\pm 1.7 \text{ mmol m}^{-2} \text{ h}^{-1}$ of CO_2 at salinity
509 lower than 3 and absorbs $-1.3\pm 0.6 \text{ mmol m}^{-2} \text{ h}^{-1}$ of CO_2 between salinities 3 and 34. A precise
510 integration of these fluxes would require an estimate of the relative surface area of different salinity
511 ranges according to the shape of the $p\text{CO}_2$ bell curve. In particular, it is necessary to separate the
512 0-3 salinity range that behaves as a source (as does the river) from the estuarine waters with
513 salinities above 3 that behave as a sink (Table 1). During our study, we could sample the marine
514 end-member in the shallow waters of the mouth of the estuary at high tide (Fig. S1). However, at
515 low tide as well as on average over the tidal cycle, salinity at the mouth is generally lower, and a
516 significant part of the salinity gradient occurs in a plume offshore. Based on numerical modelling,
517 Cavalcante et al. (2020) showed that the tide-integrated salinity at the mouth of the São Francisco
518 Estuary can be as low as 22 during concomitant neap tides and high river flow. In addition, surface
519 waters with salinities lower than 34 extends 5-20km offshore, with a surface area up to 50km^2 , that
520 is, an area much larger than the 19km^2 of the inner estuary (Cavalcante et al. 2020). Considering
521 the low river discharge during the study period, an area of 6km^2 for the 0-3 salinity range, which
522 corresponds to one third of the inner estuary, emits 4.3tC per day. An area 30 km^2 (13km^2 in the
523 inner estuary and 17km^2 in the plume offshore) for the 3-34 salinity range will absorb -11.2tC per
524 day. With these hypotheses on the surface areas, the São Francisco Estuary absorbs 7tC per day
525 of CO_2 . In comparison, the input of DIC by the river was 95 and 70 tC per day, respectively in Aug.
526 2014 and Nov. 2015. Consequently, the invasion of CO_2 from the atmosphere due to
527 thermodynamics during mixing will increase the DIC export to the sea by 7-10%. This modest
528 increase in the DIC discharge of the São Francisco Estuary to the ocean might be also partly
529 explained by its morphology and hydrological feature induced by very shallow depths at the mouth
530 and a very steep longitudinal salinity gradient between 10 and 25 inside the lagoon (Fig. 4).

531

532 By calculating for each salinity increment the quantity of CO₂ absorbed from the atmosphere during
533 the residence time of waters in the estuary, our mixing Ex-pCO₂ model provides a precise
534 evaluation of the impact of gas exchange on the C-pCO₂ curves (Fig. 5). Evasion occurs first at low
535 salinity, and the correction is negative during a restricted amount of time; invasion occurs at salinity
536 above 3-5 with a positive correction and presumably during a longer amount of time. In the case of
537 the São Francisco Estuary, with a water depth of 3m, a residence time of half a day and relatively
538 low wind speed values (Table 1), the model results in a difference between C-pCO₂ and Ex-pCO₂
539 of only 4ppmv in the 3-30 salinity range in Nov. 2015, corresponding to ~10% of the O-pCO₂
540 deviation above the C-pCO₂ mixing curve. However, strong stratification of the water column at
541 intermediate salinities may alter this conclusion in two opposite ways: on one hand, if we consider
542 a mixed surface layer of only 1m height as representative in-situ conditions (Cavalcante et al.
543 2017), CO₂ invasion will generate a larger difference between Ex-pCO₂ and C-pCO₂, on average
544 ~12ppmv, which corresponds to ~25% of the O-pCO₂ deviation above the C-pCO₂ mixing curve at
545 salinity > 3 in Nov. 2015; on the other hand, stratification of the water column implies that part of
546 the mixing of estuarine water occurs below the water surface, that is, without contact with the
547 atmosphere and without gas exchange. Wind speed, fetch length, and water current all contribute
548 to surface turbulence in estuaries, where gas exchange is generally faster than in the ocean
549 (Borges et al., 2004; Orton et al., 2010). Most of the proposed k_{600} parameterization in estuaries
550 are based on data in relatively well-mixed estuaries (Borges et al., 2004; Abril et al., 2009; Orton et
551 al., 2010). To our best knowledge, no gas exchange study has been performed in highly stratified
552 systems, where buoyancy fluxes dissipate kinetic energy as turbulence (Etemad-Shahidi and
553 Imberger, 2002) potentially enhancing gas exchange, whereas stratification limits the vertical
554 diffusion of atmospheric CO₂ to the whole water column. In large tropical estuaries and plumes
555 such as the Amazon and the Congo, most of the salinity gradient occurs offshore where wind
556 speed is higher. Gas exchange in these plumes can significantly alter the C-pCO₂ mixing curves
557 and the impact of stronger wind and longer residence time in the mixing zone might be partially
558 offset by a deeper mixed layer in the range of 5-30 m (Grotsky et al., 2014; Phillipson and Toumi,
559 2020).

560

561 4.5. Relative contributions of $p\text{CO}_2$ deviations from conservative mixing

562 In August 2014 in the main channel of the São Francisco estuary, heating and tidal pumping were
563 almost negligible and we found little deviation of $O\text{-}p\text{CO}_2$ from $C\text{-}p\text{CO}_2$, except in the salinity range
564 0-3, where the $O\text{-}p\text{CO}_2$ were on average 45 ppmv lower than the modelled conservative $p\text{CO}_2$
565 (Fig. 3A), suggesting the occurrence of autotrophic activity by phytoplankton and/or CO_2 evasion in
566 the area, consistent with observations at low tides in Nov. 2015 during the 25h cycle (Fig. 4). In
567 contrast, the deviation from conservative mixing was more pronounced in Nov. 2015, during
568 summer and spring tides, and we could calculate the distribution of the three major active
569 processes that make $p\text{CO}_2$ deviate from the conservative curve along the salinity gradient, that is,
570 (i) surface water heating or cooling based on temperature field data ($T\text{-}p\text{CO}_2$), (ii) evasion or
571 invasion of CO_2 based on modelling ($\text{Ex-}p\text{CO}_2$), and (iii) autotrophy or the sum of heterotrophy and
572 tidal pumping from mangrove creeks as the residual part of the deviation between modelled and
573 observed data, calculated as $O\text{-}p\text{CO}_2 - T\text{-}p\text{CO}_2 - \text{Ex-}p\text{CO}_2$ (Cotovicz et al. 2020). We have binned
574 our Nov. 2015 data, calculating the means and standard deviations of $O\text{-}p\text{CO}_2$ and $T\text{-}p\text{CO}_2$ for
575 each salinity increment. In Aug. 2014, the deviation of $p\text{CO}_2$ from conservative mixing was too low
576 (Table 1). The difference between $O\text{-}p\text{CO}_2$, $C\text{-}p\text{CO}_2$, $T\text{-}p\text{CO}_2$ and $\text{Ex-}p\text{CO}_2$ were within the
577 uncertainties of measurements and calculations, meaning that thermodynamics alone drives
578 almost all the $O\text{-}p\text{CO}_2$ distribution. The 2015 binned $O\text{-}p\text{CO}_2$ and $T\text{-}p\text{CO}_2$ could be compared with
579 the modelled $C\text{-}p\text{CO}_2$ and $\text{Ex-}p\text{CO}_2$ (Fig. 6). We also separated the day and night periods for the
580 regions with salinities above and below 3 and we calculated the CO_2 fluxes corresponding to these
581 three processes (heating, gas exchange and the residual as biological activity) using wind speed
582 data and three gas transfer parameterizations (Table 2). The calculations indicate that in Nov.
583 2015, heating was consistently stronger at daytime compared to night-time, and contributed to a
584 peak at 20 ppmv at salinity 28 (Fig. 6), and a maximum average deviation from conservativity of
585 +12 ppmv at daytime and salinity above 3, corresponding to a heating CO_2 flux of $0.2 \text{ mmol m}^{-2} \text{ h}^{-1}$
586 (Table 2). Gas exchange had a slightly lower impact on $p\text{CO}_2$ values than heating, with rapid
587 evasion of river-borne CO_2 occurring at low salinity and CO_2 invasion at salinity between 3 and 34.
588 According to our quantitative analysis, concomitant CO_2 evasion and net autotrophy occur in the 0-
589 3 salinity range, whereas concomitant CO_2 invasion and net heterotrophy associated to tidal

590 pumping from mangroves occur at salinity above 3 (Fig. 6). This trend in the São Francisco
591 Estuary is similar to the one recently reported in the mesotrophic Paraíba do Sul Estuary during
592 high river discharge (Cotovicz et al. 2020). These two river-dominated tropical estuaries have low
593 TA concentrations in the river end-member. At low salinities, inputs of river-borne CO₂ combined
594 with low buffering capacity favour outgassing, whereas little salinity stress allows some production
595 of freshwater phytoplankton (Cloern, 1996; Lancelot and Muylaert, 2012; Cotovicz et al., 2020). At
596 salinities below 3, the O-*p*CO₂ values were 109 ppmv below the modelled C-*p*CO₂ values at
597 daytime, but 34 ppmv above at night-time (Table 2), consistent with phytoplanktonic photosynthetic
598 activity. The different salinity ranges sampled at daytime (0-3) and night-time (1.4-3) do not allow
599 to accurately estimate a NEP from diurnal variations in the upper estuary. At increasing salinities,
600 the mixing with buffered seawater creates thermodynamics conditions for CO₂ invasion and offsets
601 some apparent heterotrophy combined with tidal advection of mangrove-derived CO₂. The latter
602 generates a deviation (calculated as O-*p*CO₂ – T-*p*CO₂ – Ex-*p*CO₂) of about 40 ppmv of *p*CO₂
603 along the 4-25 salinity range (Fig. 6) and +33 ppmv (daytime) and +27 ppmv (night time) on
604 average over the 3-34 salinity gradient (Table 2). Interestingly, our approach also suggests some
605 autotrophic activity in the 30-33 salinity range (Fig. 6B), which is also a classical pattern of
606 phytoplankton distribution in estuaries; indeed, blooms of marine phytoplanktonic species are a
607 common feature in high salinities regions of river plumes, where they can take benefit from the
608 available light and nutrients and from the stratification of the water column (Cloern, 1996; Lancelot
609 and Muylaert, 2012). Heating of water made O-*p*CO₂ higher than T-*p*CO₂ all along the salinity
610 gradient with a maximum difference between O-*p*CO₂ and T-*p*CO₂ of +22 ppmv at salinity 32,
611 precisely where the bloom of marine phytoplankton apparently occurred, possibly favoured by
612 warmer surface waters and a temporarily more stratified water column.

613

614 After a conversion to CO₂ fluxes by applying a gas transfer velocity, the deviation between the T-
615 *p*CO₂ and the modelled Ex-*p*CO₂ corrected for gas exchange, provide an indirect and integrative
616 estimate of NEP (Table 2). Quantitatively, the computed NEP (including tidal pumping) with this
617 original method in the São Francisco (Table 2), as well as in the Paraíba do Sul (Cotovicz et al.,
618 2020) are around 1 or less mmol m⁻² h⁻¹, when NEP reported in estuaries of the world varies

619 between +5 (autotrophy) and -12 mmol m⁻² h⁻¹ (heterotrophy) (Borges and Abril 2011). Despite
620 these low values, our method is quite sensitive and the sign and spatial distribution of the
621 calculated NEP are consistent with classical concepts of estuarine plankton ecology (Crump et al.,
622 2004; Lancelot and Muylaert, 2012), tidal advection and the short residence-time in the mixing
623 zone. This confirms the robustness of our approach that could be applied to many estuarine
624 environments, whether they act as CO₂ sink or source.

625

626

627 **5. Conclusions**

628 The São Francisco Estuary displays specific conditions in terms of carbonate chemistry and air-
629 water CO₂ exchange: because of warm and poorly buffered freshwaters, oligotrophic conditions
630 and short residence time, carbonate thermodynamic equilibration during mixing predominate over
631 biological processes and determine water pCO₂ and air-water CO₂ fluxes. This results in an abiotic
632 uptake of atmospheric CO₂ by the estuary at salinities above 3 in the main channel and the DIC
633 export to the sea is increased by 7-10%. During winter and neap tide period, tidal pumping and
634 heating were weak and the observed pCO₂ almost matched the theoretical conservative mixing
635 curve, within the error of measurements and computations. During summer and spring tide period,
636 the observed pCO₂ was still below the atmospheric value, but on average +49ppmv above the
637 conservative mixing curve. At that season and salinities > 3, heating of water relative to the mixing
638 of the two end-members contributed to ~15%, and gas exchange contributed to ~10% of the
639 deviation of observed pCO₂ from conservativity, the remaining ~75% being attributed in majority to
640 tidal pumping from mangroves and brackish marshes, maybe with some respiratory activity in
641 estuarine waters despite the short residence time. Following the approach of Cotovicz et al. (2020)
642 in the mesotrophic and tropical Paraíba do Sul River delta that also behaves as a CO₂ sink in the
643 mixing zone, our study is a second detailed report of CO₂ air-water exchange, based on the
644 combination of high-resolution pCO₂ field data and theoretical computation that cover the complete
645 salinity gradient. We highlight a singular situation, not only occurring in the oligotrophic São
646 Francisco, but also the mesotrophic Paraíba do Sul Estuary, of concomitant CO₂ uptake and
647 heterotrophy at salinities higher than 3. Similar thermodynamics conditions, i.e., warm and poorly

648 buffered freshwaters that potentially generates CO₂ invasion in the mixing zone, occur in large
649 tropical river plumes like the Amazon, Congo and Orinoco. High resolution pCO₂ measurements
650 along the entire salinity gradient of these large estuaries and plumes are thus necessary. In the
651 Amazon plume, the available equilibrator pCO₂ data covers only the >17 salinities range with
652 undersaturated values with respect to the atmosphere, well below those predicted by the
653 conservative mixing of Amazon river water with Atlantic equatorial water (Körtzinger, 2003; Lefèvre
654 et al., 2017). This indicates that in the Amazon, thermodynamic and biological processes
655 contribute together to CO₂ invasion because the plume is autotrophic, whereas in the Paraíba do
656 Sul and São Francisco Estuaries, the two processes are competing with each other both at low
657 salinities (evasion and autotrophy) and high salinities (invasion and heterotrophy). High-resolution
658 surface pCO₂, temperature and salinity measurements coupled with modelling of estuarine mixing
659 provided some detailed and precise information that could be applied in many plumes of large
660 tropical rivers that contribute more significantly to the riverine carbon load to the world ocean.

661

662 **Acknowledgements**

663 This research was funded by the Brazilian National Council of Research and Technological
664 Development (CNPq) through the Science without border program (PVE 401726-6), the *Instituto*
665 *do Milênio Estuários* project (420.050/2005-1) and the National Institute of Science and
666 Technology *Transferências de Materiais Continente-Oceano* (TCMOcean 573.601/2008-9).
667 Georganes H Cavalcante was supported by the American University of Sharjah (research Grant
668 FRG19-M-G74). This work is also a contribution to the International Research Project *Vulnérabilité*
669 *des Ecosystèmes Littoraux Tropicaux face à l'Eutrophisation* funded by the French National Centre
670 for Scientific Research (CNRS-INEE).

671

672 **6. References**

- 673 Abril G. and Frankignoulle M. (2001) Nitrogen-Alkalinity interactions in the highly polluted Scheldt
674 basin (Belgium). *Water Res.* **35**, 844-850.
- 675 Abril G., Commarieu M.V., Sottolichio A., Bretel P. and Guérin F. (2009) Turbidity limits gas
676 exchange in a large macrotidal estuary. *Estuar. Coast. Shelf Sci.* **83**, 342–348.

677 Abril G., Etcheber H., Borges A. V. & Frankignoulle M. (2000) Excess atmospheric carbon dioxide
678 transported by rivers into the Scheldt Estuary. *C. R. Acad. Sci. Paris Série IIA* **330**, 761-768.

679 Abril, G., Etcheber, H., Delille, B., Frankignoulle, M., Borges, A. V., (2003). Carbonate dissolution
680 in the turbid and eutrophic Loire estuary. *Mar. Ecol. Prog. Ser.* **259**, 129-138.

681 Bauer J. E., Cai W. J., Raymond P., Bianchi T. S., Hopkinson C. S. and Regnier P. G. (2013) The
682 changing carbon cycle of the coastal ocean. *Nature* **504**, 61–70.

683 Bernardes, L. M. C., (1951). Notas sobre o clima da bacia do Rio são Francisco. *Rev. Bras.*
684 *Geogr.* **13**, 473–489.

685 Bernardes, M. C., Knoppers, B. A., Rezende, C. E., Souza, W. F. L., Ovalle, A. R. C. (2012). Land-
686 sea interface features of four estuaries on the South America Atlantic coast. *Braz. J. Biol.*,
687 **72**, 761-774. [dx.doi.org/10.1590/S1519-69842012000400011](https://doi.org/10.1590/S1519-69842012000400011).

688 Borges A. V. and Abril G. (2011) Carbon dioxide and methane dynamics in estuaries. In *Treatise*
689 *on estuarine and coastal science* (eds. E. Wolanski and D. D. McLusky), vol 5, Academic
690 Press, Amsterdam. pp. 119–161.

691 Borges A. V., Schiettecatte L.-S., Abril G., Delille B. and Gazeau F. (2006) Carbon dioxide in
692 European Coastal waters. *Estuar. Coast. Shelf Sci.* **70**, 375-387.

693 Borges, A. V., Djenidi, S., Lacroix, G., Theate, J., Delille, B., Frankignoulle, M. (2003).
694 Atmospheric CO₂ flux from mangrove surrounding waters. *Geophys. Res. Lett.* **30**, 1558.

695 Borges, A. V., Delille, B., Schiettecatte, L.-S., Gazeau, F., Abril, G., Frankignoulle M., (2004). Gas
696 transfer velocity of CO₂ in three European estuaries (Randers Fjord, Scheldt and Thames).
697 *Limnol. Oceanogr.* **49**, 1630-1641.

698 Borges, A.V. (2005). Do we have enough pieces of the jigsaw to integrate CO₂ fluxes in the
699 Coastal Ocean? *Estuaries* **28**, 3-27.

700 Bouillon S., Frankignoulle M., Dehairs F., Velimirov B., Eiler A., Abril G., Etcheber H. & Borges
701 A.V. (2003) Inorganic and organic carbon biogeochemistry in the Gautami Godavari estuary
702 (Andhra Pradesh, India) during pre-monsoon: the local impact of extensive mangrove
703 forests. *Global Biogeochem. Cy.* **17**, 1114.

704 Cai W. J. (2011) Estuarine and coastal ocean carbon paradox: CO₂ sinks or sites of terrestrial
705 carbon incineration? *Ann. Rev. Mar. Sci.* **3**, 123–145.

- 706 Cai W. J., Chen A. C., and Borges A. V. (2013). Carbon dioxide dynamics and fluxes in coastal
707 waters influenced by river plumes. In *Biogeochemical Dynamics at Major River-Coastal*
708 *Interfaces: Linkages with Global Change* (eds. T. Bianchi, M. Allison, and W. Cai) Cambridge
709 University Press. pp. 155-173. doi:10.1017/CBO9781139136853.010
- 710 Cavalcante G., Miranda L.B., and Medeiros P. R. P. (2017) Circulation and salt balance in the São
711 Francisco river Estuary (NE/Brazil). *Revista Brasileira de Recursos Hídricos*, **22**.
712 doi.org/10.1590/2318-0331.021720170003.
- 713 Cavalcante G., Vieira F., Campos E., Brandini N., Medeiros P.R.P. (2020) Temporal streamflow
714 reduction and impact on the salt dynamics of the São Francisco River Estuary and adjacent
715 coastal zone (NE/Brazil). *Regional Studies in Marine Science* 38: 101363.
716 doi.org/10.1016/j.rsma.2020.101363.
- 717 Chen C. T. A. and Borges A. V. (2009) Reconciling opposing views on carbon cycling in the
718 coastal ocean: continental shelves as sinks and near-shore ecosystems as sources of
719 atmospheric CO₂. *Deep Sea Res. Part 2 Top. Stud. Oceanogr.* **56**, 578-590.
- 720 Cloern J. E. (1996) Phytoplankton bloom dynamics in coastal ecosystem: a review with some
721 general lessons from sustained investigation of San Francisco Bay, California. *Rev.*
722 *Geophys.* 34: 127-168.
- 723 Cotovicz Jr., L. C., Knoppers B. A., Brandini N., Costa Santos S. J. and Abril G. (2015) A strong
724 CO₂ sink enhanced by eutrophication in a tropical coastal embayment (Guanabara Bay, Rio
725 de Janeiro, Brazil). *Biogeosciences* **12**, 6125–6146.
- 726 Cotovicz Jr., L.C., Libardoni, B., Brandini, N., Knoppers, B., Abril, G. (2016) Comparações entre
727 medições em tempo real da pCO₂ aquática com estimativas indiretas em dois estuários
728 tropicais contrastantes: o estuário eutrofizado da Baía de Guanabara (RJ) e o estuário
729 oligotrófico do Rio São Francisco (AL). *Quím. Nova* **39**, 1206–1214
- 730 Cotovicz Jr., L. C., Vidal, L. O., de Rezende, C. E., Bernardes, M. C., Knoppers, B. A., Sobrinho,
731 R., L., Cardoso, R. P., Muniz, M., dos Anjos, R. M., Biehler, A., Abril, G. (2020) Carbon
732 dioxide sources and sinks in the delta of the Paraíba do Sul River (Southeastern Brazil)
733 modulated by carbonate thermodynamics, gas exchange and ecosystem metabolism during
734 estuarine mixing. *Mar. Chem.* **226** (20), 103869.

735 Cotovicz Jr., L. C., Ribeiro, R., Régis, C. R., Bernardes, M., Sobrinho, R., Vidal, L. O., Tremmel,
736 D., Knoppers, B. A., Abril, G. (2021) Greenhouse gas emissions (CO₂ and CH₄) and
737 inorganic carbon behavior in an urban highly polluted tropical coastal lagoon (SE, Brazil).
738 *Environ. Sci. Pollut. Res.*, doi: 10.1007/s11356-021-13362-2

739 Crump, B. C., Hopkinson, C. S., Sogin, M. L. and Hobbie, J. E. (2004) Microbial biogeography
740 along an estuarine salinity gradient: combined influences of bacterial growth and residence
741 time. *Appl. Environ. Microbiol.* **70**, 1494-1505.2

742 de Jong, P., Tanajura, C. A. S., Sánchez, A. S., Dargaville, R., Kiperstok, A., Torres, E. A (2018).
743 Hydroelectric production from Brazil's São Francisco River could cease due to climate
744 change and inter-annual variability. *Sci. Total Environ.* **634**, 1540-1553.

745 Delaigue L., Thomas H., and Mucci A. (2020) Spatial variations in CO₂ fluxes in the Saguenay
746 Fjord (Quebec, Canada) and results of a water mixing model. *Biogeosciences*, 17, 547–566,
747 doi:10.5194/bg-17-547-2020

748 Dickson, A. G., Millero, F. J. (1987). A comparison of the equilibrium constants for the dissociation
749 of carbonic acid in seawater media. *Deep-Sea Res.* **34**, 1733–1743.

750 Dinauer, A. ; Mucci, A. (2017). Spatial variability in surface-water pCO₂ and gas exchange in the
751 world's largest semi-enclosed estuarine system: St. Lawrence Estuary (Canada).
752 *Biogeosciences*, 14, 3221-3237.

753 Dominguez, J. M. L., (1996). The São Francisco strandplain: a paradigm for wave-dominated
754 deltas? *Geology Society London, Spec. Publ.* **117**, 217–231.

755 Etemad-Shahidi A. and Imberger J. (2002) Anatomy of turbulence in a narrow and strongly
756 stratified estuary. *J. Geophys. Res.* **107**, 3070, doi10.1029/2001JC000977

757 Frankignoulle M., Abril G., Borges A., Bourge I., Canon C., Delille B., Libert E. and Théate J. M.
758 (1998) Carbon dioxide emission from European estuaries. *Science* **282**, 434-436.

759 Frankignoulle M., Bourge I., and Wollast R. (1996) Atmospheric CO₂ fluxes in a highly polluted
760 estuary (The Scheldt), *Limnol. Oceanogr.* **41**, 365-369.

761 Frankignoulle, M., Borges, A. V., and Biondo, R. (2001) A new design of equilibrators to monitor
762 carbon dioxide in highly dynamic and turbid environments. *Water Res.* **35**, 1344–1347.

763 Grodsky S. A., Reverdin G., Carton J.A. and Coles V. J. (2014) Year-to-year salinity changes in
764 the Amazon plume: Contrasting 2011 and 2012 Aquarius/SACD and SMOS satellite data
765 *Remote Sens. Envir.* **140**, 14-22.

766 Hunt, C. W., Salisbury, J. E. and Vandemark, D.: Contribution of non-carbonate anions to total
767 alkalinity and overestimation of pCO₂ in New England and New Brunswick rivers.
768 *Biogeosciences*, 8, 3069–3076, 2011.

769 Körtzinger A. (2003). A significant CO₂ sink in the tropical Atlantic Ocean associated with the
770 Amazon river plume. *Geophys. Res. Lett.* **30**, 2287, doi:10.1029/2003GL018841.

771 Lancelot, C., Muylaert, K. (2012). Trends in Estuarine Phytoplankton Ecology. In *Treatise on*
772 *estuarine and coastal science* (eds. E. Wolanski and D. D. McLusky), Vol 7, Academic
773 Press, Amsterdam. pp. 5-15.

774 Lefèvre N., Flores Montes M., Gaspar F. L., Rocha C., Jiang S., De Araújo M. C. and Ibánhez J. S.
775 P. (2017) Net Heterotrophy in the Amazon Continental Shelf Changes Rapidly to a Sink of
776 CO₂ in the Outer Amazon Plume. *Front. Mar. Sci.* **4**, 278. doi:0.3389/fmars.2017.00278

777 Leopold A., Marchand C., Deborde J. and Allenbach M. (2016) Water Biogeochemistry of a
778 Mangrove-Dominated Estuary Under a Semi-Arid Climate (New Caledonia). *Estuar. Coast.*
779 **40**, 773-791.

780 Maher D. T., Call M., Santos I. R., Sanders C. (2018) Beyond burial: lateral exchange is a
781 significant atmospheric carbon sink in mangrove forests. *Biol. Lett.* **14**,
782 doi :10.1098/rsbl.2018.0200

783 Maher D. T., Santos I. R., Golsby-Smith L., Gleeson J. and Eyre B. D. (2013) Groundwater-derived
784 dissolved inorganic and organic carbon exports from a mangrove tidal creek: The missing
785 mangrove carbon sink? *Limnol. Oceanogr.* **58**, 475–488.

786 Medeiros P. R. P., Knoppers B. A., dos Santos Júnior R. C. and de Souza W.F.L. (2007) Aporte
787 fluvial e dispersão de matéria particulada em suspensão na zona costeira do Rio São
788 Francisco (SE/AL) *Geochimica Brasiliensis*, 21(2)212 - 231, 2007.

789 Medeiros P. P. M., Knoppers B. A., Cavalcante G. H., de Souza W. F. L. (2011) Changes in
790 Nutrient Loads (N, P and Si) in the São Francisco Estuary after the Construction of Dams.
791 *Braz. Arch. Biol. Technol.* **54**, 387-397.

792 Medeiros P. R. P., Cavalcante G. H. , Melo E. R. and Brandini N. (2018) The são Francisco river
793 (NE): review on the interannual loading of particulate matter suspended to the ocean and
794 impacts of dams. *Int. J. Hydrol.* **2**,190-193. doi:10.15406/ijh.2018.02.00067

795 Mehrbach C., Culberson, C. H. Hawley J. E., Pytkowicz R.M. (1973). Measurements of the
796 apparent dissociation constants of carbonic acid in seawater at atmospheric pressure.
797 *Limnol. Oceanogr.* **18**, 897–907.

798 Melo, E. R., Brandini, N., Medeiros, P. R. P., Silva, R., and Cavalcante, G. (2020). Nutrients Load
799 Estimation in a Regulated Streamflow Estuary: The São Francisco Estuary (NE/Brazil).
800 *Revista Brasileira de Meteorologia.* 35, 803-811.

801 Melo-Magalhães E.M., Moura A.N., Medeiros P.R.P. and Koenig M.L. (2015) Microphytoplankton
802 biomass and trophic state of the estuarine region of the São Francisco River (Northeastern
803 Brazil) *Braz. J. Aquat. Sci. Technol.*, **20**, 19-30.

804 Murgulet, D., Trevino M., Douglas A., Spalt N., Hu X., and Murgulet V. (2018). Temporal and
805 spatial fluctuations of groundwater-derived alkalinity fluxes to a semiarid coastal embayment.
806 *Sci. Total Environ.* **630**, 1343–59. doi:10.1016/j.scitotenv.2018.02.333

807 Neubauer S.C., Anderson, I.C. (2003). Transport of dissolved inorganic carbon from a tidal
808 freshwater marsh to the York River estuary. *Limnol. Oceanogr.* **48**, 299-307.

809 Orton P.M. Zappa C.J. and McGillins W.R. (2010) Tidal and atmospheric influences on near-
810 surface turbulence in an estuary. *J. Geophys. Res.* **115**: C12029,
811 doi:10.1029/2010JC006312.

812 Phillipson L. and Toumi R. (2020) Assimilation of Satellite Salinity for Modelling the Congo River
813 Plume. *Remote Sens.* **12**, 11; doi:10.3390/rs12010011

814 Pierrot D., Lewis D. E., and Wallace D. W. R. (2006). MS Excel Program Developed for CO2
815 System Calculations. ORNL/CDIAC-105a. Carbon Dioxide Information Analysis Center, Oak
816 Ridge National Laboratory, U.S. Department of Energy, Oak Ridge, Tennessee. doi:
817 10.3334/CDIAC/otg.CO2SYS_XLS_CDIAC105a

818 Raymond P.A., Cole J. J. (2001). Gas exchange in rivers and estuaries: choosing a gas transfer
819 velocity. *Estuaries* **24**: 312-317.

820 Santos, I. R., Maher, D. T., Larkin, R., Webb, J., Sanders, C. J. (2018) Carbon outwelling and
821 outgassing vs. burial in an estuarine tidal creek surrounded by mangrove and saltmarsh
822 wetlands. *Limnol. Oceanogr. Letters* **2**, 1-18. doi.org/10.1002/lno.11090.

823 Sarma, V., Viswanadham, R., Rao, G. D., Prasad, V. R., Kumar, B. S. K., Naidu, S. A., Kumar, N.
824 A., Rao, D. B., Sridevi, T., Krishna, M. S., Reddy, N. P. C., Sadhuram, Y., Murty, T. V. R.
825 (2012) Carbon dioxide emissions from Indian monsoonal estuaries, *Geophys. Res. Lett.*, **39**,
826 L03602, doi:10.1029/2011gl050709.

827 Smith S.V. and Hollibaugh J.T. (1993). Coastal metabolism and the oceanic carbon balance. *Rev.*
828 *Geophys.* **31**, 75-89.

829 Takahashi T., Sutherland S. C., Sweeney C., Poisson A., Metzl N., Tilbrook B., Bates N.,
830 Wanninkhof R., Feely R. a., Sabine C., Olafsson J. and Nojiri Y. (2002) Global sea-air CO₂
831 flux based on climatological surface ocean pCO₂, and seasonal biological and temperature
832 effects. *Deep. Sea Res. Part II* **49**, 1601–1622.

833 Wanninkhof, R. (1992). Relationship between wind speed and gas exchange over the ocean. *J.*
834 *Geophys. Res.* **97**, 7373-7382.

835 Weiss R. F. (1974). Carbon dioxide in water and seawater: the solubility of a non-ideal gas. *Mar.*
836 *Chem.* **2**, 203–215.

837 Whitfield, M. and Turner D. R. (1986) The carbon dioxide system in estuaries – An inorganic
838 perspective. *Sci. Total Environ.* **49**, 235-255.

839 Wollast R. (1991). The coastal organic carbon cycle: fluxes, sources, and sinks. In *Ocean Margin*
840 *Processes in Global Change* (eds. Mantoura, R. F. C., Martin, J.M., Wollast, R.) Wiley,
841 Chichester, West Sussex, England, pp. 365–381.

842 Yao H. and Hu X. (2017) Responses of carbonate system and CO₂ flux to extended drought and
843 intense flooding in a semiarid subtropical estuary. *Limnol. Oceanogr.* **62** S112-S130.

844 Yao H., McCutcheon M.R., Staryk C.J. and Hu X. (2020) Hydrologic controls on CO₂ chemistry and
845 flux in subtropical lagoonal estuaries of the northwestern Gulf of Mexico. *Limnol. Oceanogr.*
846 **9999**, 2020, 1–19. doi:10.1002/lno.11394.

847

848

849

850

851

852

853

Table 1. Synthesis of measured and calculated parameters during the two cruises. O- $p\text{CO}_2$ is the observed $p\text{CO}_2$ as measured *in situ*, C- $p\text{CO}_2$ is the conservative $p\text{CO}_2$ modelled from mixing of river water with seawater, T- $p\text{CO}_2$ is the $p\text{CO}_2$ normalized to temperature resulting from the mixing of the two end-members and Ex- $p\text{CO}_2$ is the $p\text{CO}_2$ resulting from conservative after being corrected for gas exchange. *Calculated using the mixing/gas exchange model described in Fig.5, for the measured U10, a value of RT of 0.5 days and H of 3m. # During night, measured and modelled conservative $p\text{CO}_2$ values are lower than expected when compared to the daytime, because night-time measurements did not include samples with salinities lower than 1.2 and highest $p\text{CO}_2$. \$In order to account for the protection of mangrove trees to creek waters, we divided by 2 the wind speed values to calculate CO_2 fluxes from the mangrove secondary channel, as a first approximation. Standard deviation of the differences between two numbers were calculated as the square root of the sum of the squares of the two errors.

	Aug. 2014			Nov. 2015				Mangrove
	Main Channel		Mangrove	Main Channel				
	S<3 Day	S>3 Day	S>3 Day	S<3 Day	S<3 Night [#]	S>3 Day	S>3 Night	
Number of measurements	321	190	324	518	260	701	441	528
Temperature (°C)	26.6±0.2 26.1-27.0	26.5±0.1 26.4-26.7	26.7±0.4 26.1-27.3	28.3±0.4 27.5-29.2	27.9±0.2 27.6-28.2	28.1±0.4 27.0-28.9	27.7±0.5 26.8-28.4	28.3±0.9 26.3-29.8
O-pCO ₂ (ppmv)	752±308 245-2137	279±34 224-355	512±191 298-975	426±141 233-1040	421±60 304-514	344±39 259-423	311±30 267-383	976±314 307-2007
C-pCO ₂ (ppmv)	634±92 371-710	282±33 233-343	296±36 232-368	542±123 318-646	392±34* 298-476	295±46 238-411	275±31 238-363	334±41 238-406
T-pCO ₂ (ppmv)	753±311 245-2166	279±34 224-357	503±185 293-949	421±144 228-1043	420±61 299-512	332±37 252-405	307±29 264-373	917±292 297-1956
Ex-pCO ₂ (ppmv)	622±95 357-692	284±34 236-344	-	530±125 307-635	386±36* 294-472	299±47 238-411	280±32 241-369	-
O-pCO ₂ – C-pCO ₂ (ppmv)	117±256 -243-1444	-3±13 -65-69	216±180 40-680	-104±90 -413-407	29±21 -64-101	49±39 -31-141	36±22 -41-111	643±320 -11-1671
O-pCO ₂ – T-pCO ₂ (ppmv)	-1±7 -29-9	0±1 -2-3	9±8 -1-30	5±7 -6-19	2±2 -3-6	12±8 -10-25	5±3 -3-11	59±40 -10-124
O-pCO ₂ – Ex-pCO ₂ (ppmv)*	-12±9	2±2	-	-12±9	-6±3	4±3	4±3	-
U ₁₀ (m s ⁻¹)	1.1±0.7 0.1-2.8	1.1±0.7 0.1-2.8	0.6±0.4 0.5-1.4	2.2±1.0 0.9-3.2	0.4±0.2 0.1-1.1	2.2±1.0 0.9-3.2	0.4±0.2 0.1-1.1	1.1±0.5 [§] 0.5-1.6 [§]
k ₆₀₀ (cm h ⁻¹) W92	0.6	0.6	0.2	1.6	0.1	1.6	0.1	0.5
k ₆₀₀ (cm h ⁻¹) RC01	3.4	3.4	2.9	4.1	2.2	4.1	2.2	2.8
k ₆₀₀ (cm h ⁻¹) A09	5.6	5.6	4.1	7.3	2.8	7.3	2.8	4.6
FCO ₂ W92 (mmol m ⁻² h ⁻¹)	0.74±0.30	-0.25±0.03	0.09±0.03	0.18±0.06	0.01±0.00	-0.38±0.04	-0.04±0.00	1.23±0.40
FCO ₂ RC01 (mmol m ⁻² h ⁻¹)	3.93±1.61	-1.35±0.17	1.05±0.39	0.44±0.15	0.19±0.03	-0.94±0.11	-0.78±0.07	6.55±2.11
FCO ₂ A09 (mmol m ⁻² h ⁻¹)	6.43±2.64	-2.21±0.27	1.48±0.55	0.79±0.26	0.24±0.03	-1.68±0.19	-1.01±0.10	10.72±3.45

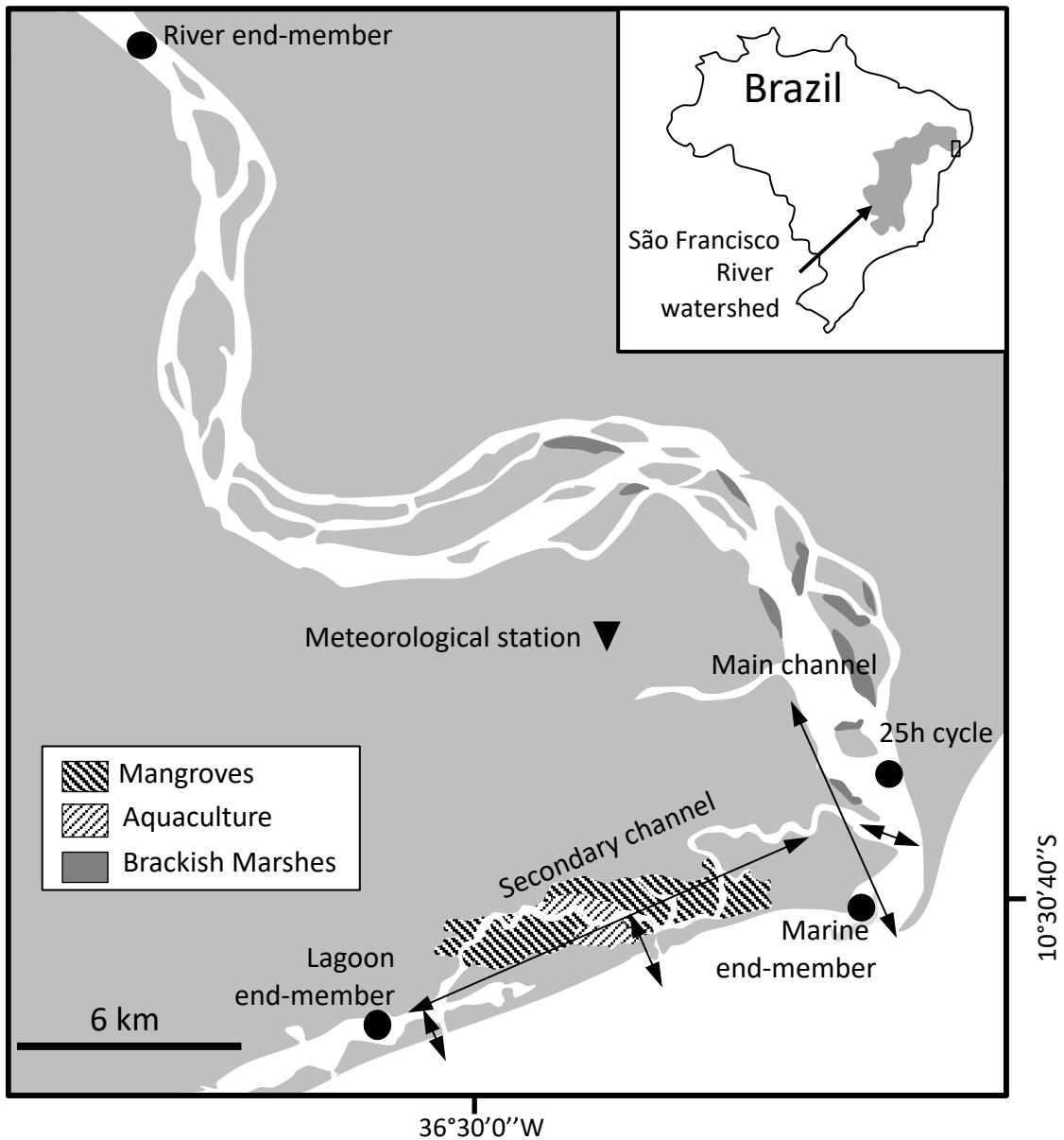
1
2 Table 2. Comparison of binned data with modelled data for the Nov. 2005 campaign. *Calculated
3 as O-*p*CO₂ minus T-*p*CO₂. #Calculated as C-*p*CO₂ minus Ex-*p*CO₂. § Calculated as
4 O-*p*CO₂ minus C-*p*CO₂ minus T-*p*CO₂ minus Ex-*p*CO₂. Standard deviation of the differences
5 between two numbers were calculated as the square root of the sum of the squares of the two
6 errors.

7

	S<3 Day	S<3 Night	S>3 Day	S>3 Night
pCO₂ (ppmv)				
Number of measurements	518	260	701	441
Salinity range	0-2.9	1.2-3.0	3.1-35.1	3.0-30.6
Temperature	28.3±0.4	27.9±0.2	28.1±0.4	27.7±0.5
O- <i>p</i> CO ₂	426±141	421±60	344±39	311±30
T- <i>p</i> CO ₂	421±144	420±61	332±37	307±29
C- <i>p</i> CO ₂	542±123	392±34	295±46	275±31
Ex- <i>p</i> CO ₂	530±123	386±35	297±46	277±31
Components of pCO₂ deviations (ppmv)				
Heating (+) / Cooling (-)*	+5±7	+2±2	+12±8	+5±3
Invasion (+) / Evasion (-)#	-12±8	-6±3	+4±3	+4±3
Heterotrophy and tidal pumping (+) / autotrophy (-) §	-97±77	+34±19	+33±25	+27±17
Sum	-104±90	+29±21	+49±39	+36±22
Gas exchange parameters				
U10 (m s ⁻¹)	2.2±1	0.4±0.2	2.2±1	0.4±0.2
k ₆₀₀ (cm h ⁻¹) W92	1.6	0.1	1.6	0.1
k ₆₀₀ (cm h ⁻¹) RC01	4.1	2.2	4.1	2.2
k ₆₀₀ (cm h ⁻¹) A09	7.3	2.8	7.3	2.8
CO₂ Fluxes (mmol m⁻² h⁻¹)				
Water-air CO ₂ flux calculated with observations	+0.47±0.31	+0.15±0.12	-1.00±0.65	-0.61±0.51
Water-air flux calculated with conservative mixing	+2.53±1.65	-0.05±0.05	-1.86±0.51	-0.86±0.72
Deviation of observations from conservative mixing	-2.06±0.97	+0.20±0.07	+0.86±0.48	+0.25±0.51
Contributions to the deviation of CO₂ fluxes (mmol m⁻² h⁻¹)				
Heating (+) / Cooling (-)	+0.10±0.06	+0.01±0.01	+0.20±0.14	+0.10±0.06
Invasion (+) / Evasion (-)	-0.21±0.14	-0.04±0.03	+0.03±0.02	+0.01±0.03
Heterotrophy plus tidal pumping (+) / autotrophy (-)	-1.94±1.31	+0.23±0.20	+0.62±0.41	+0.14±0.45

8

9

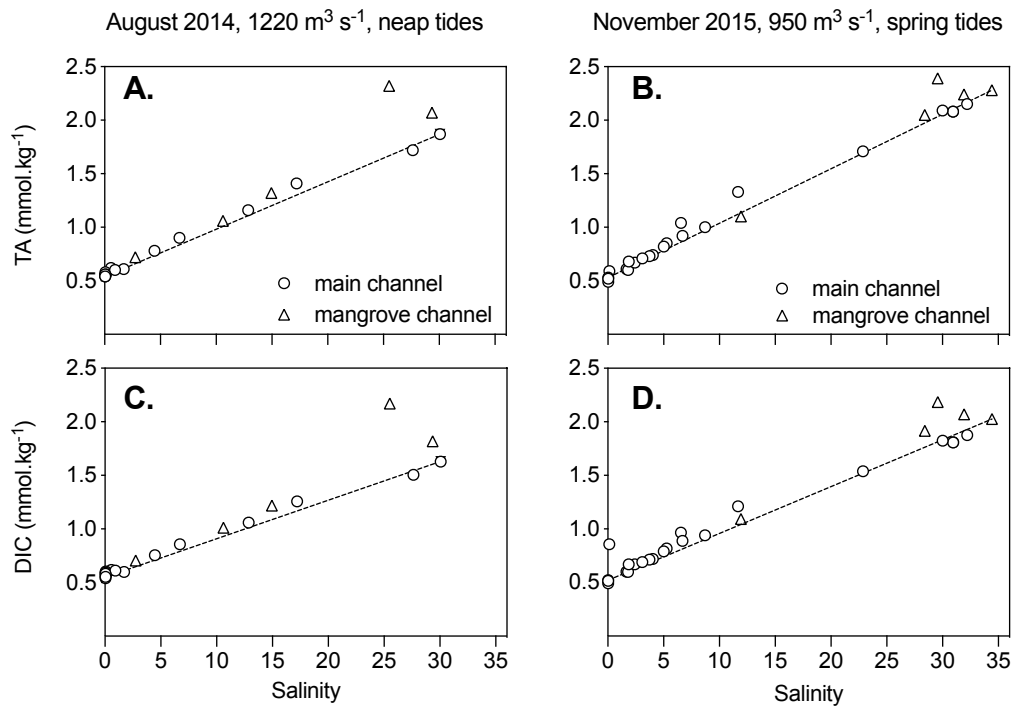


10
11
12
13
14
15
16
17

Figure 1. Map of the São Francisco Estuary. Arrows show the regions of freshwater-estuarine water-seawater mixing and the approximate localisation of the salinity gradient in the main channel, sampled from the freshwater at the centre of the river until the seawater end-member (Salinity ~ 30-34) and in the shallow tidal lagoon end-member (Salinity ~ 34).

18

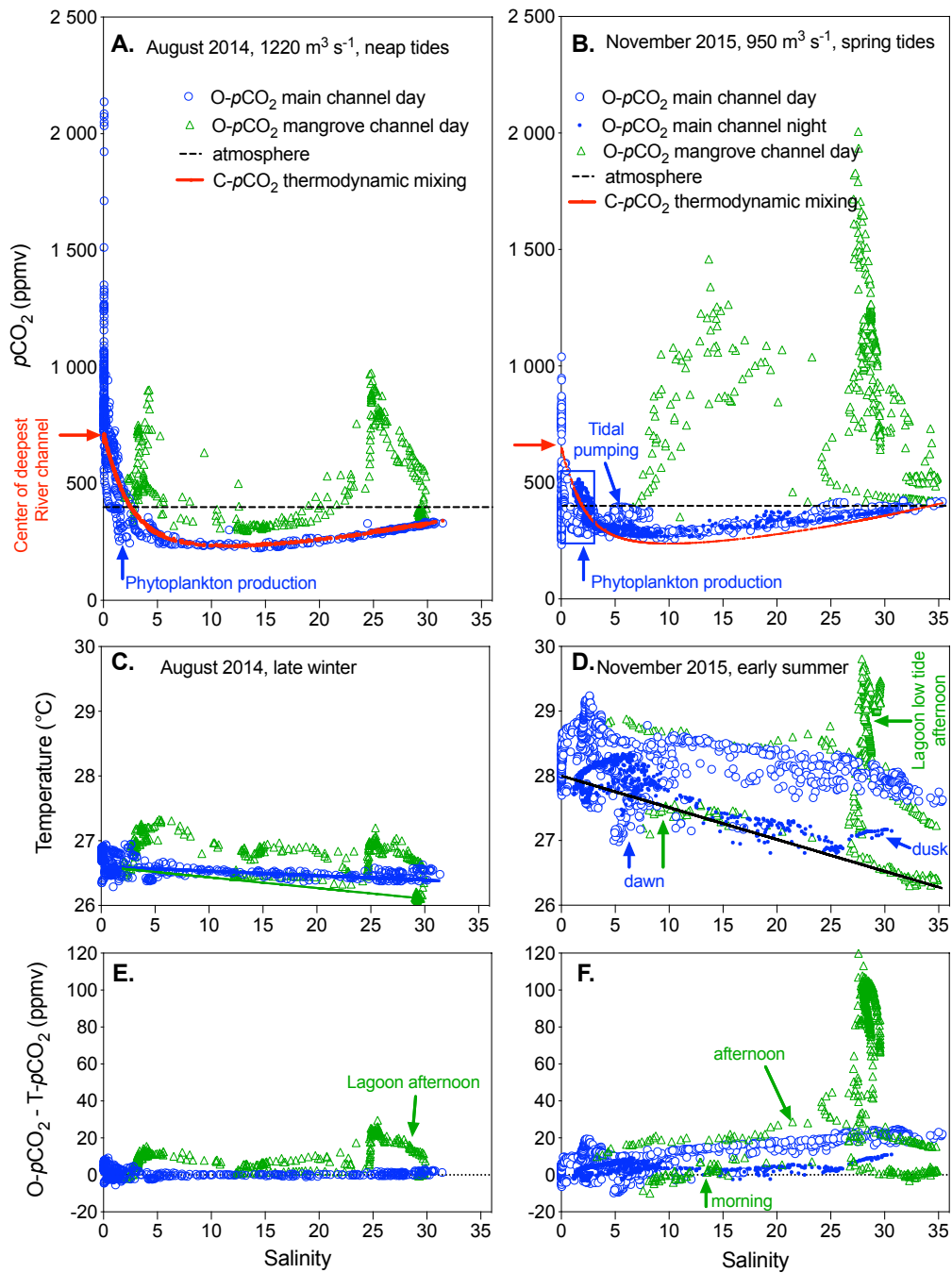
19



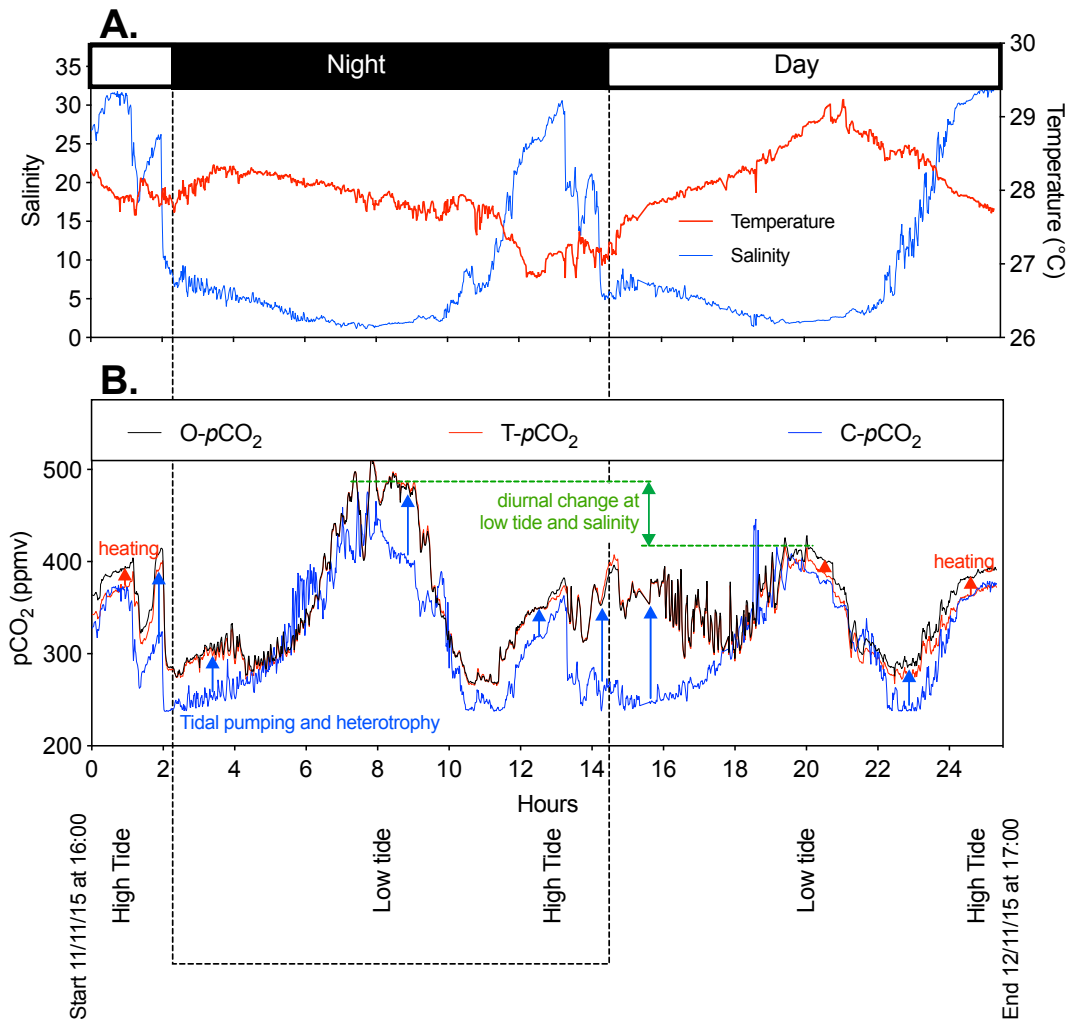
20

21 Figure 2: Distribution of Total Alkalinity (TA) (A. and B.) and Dissolved Inorganic Carbon (DIC) (C.
22 and D.) concentrations as a function of salinity in the São Francisco estuary main channel (circles)
23 and mangrove secondary channel (triangles) in August 2014 (A. and C.) and November 2015 (B.
24 and D.).

25



26
 27 Figure 3. Distribution of O-pCO₂ (A. and B.), temperature (C. and D.), and the difference between
 28 O-pCO₂ and T-pCO₂ (E. and F.) versus salinity in the São Francisco Estuary main channel (blue
 29 circles) and mangrove secondary channel (green triangles). The regression lines in panel C
 30 indicate the conservative mixing for temperature used for pCO₂ temperature normalization in the
 31 main channel (blue) and in the secondary mangrove channel (green) with a distinct marine end-
 32 member in the lagoon. The black regression line in panel D indicates the conservative mixing for
 33 temperature in the main channel and in the secondary mangrove channel with the same values in
 34 both marine end-members (see “results”).



36

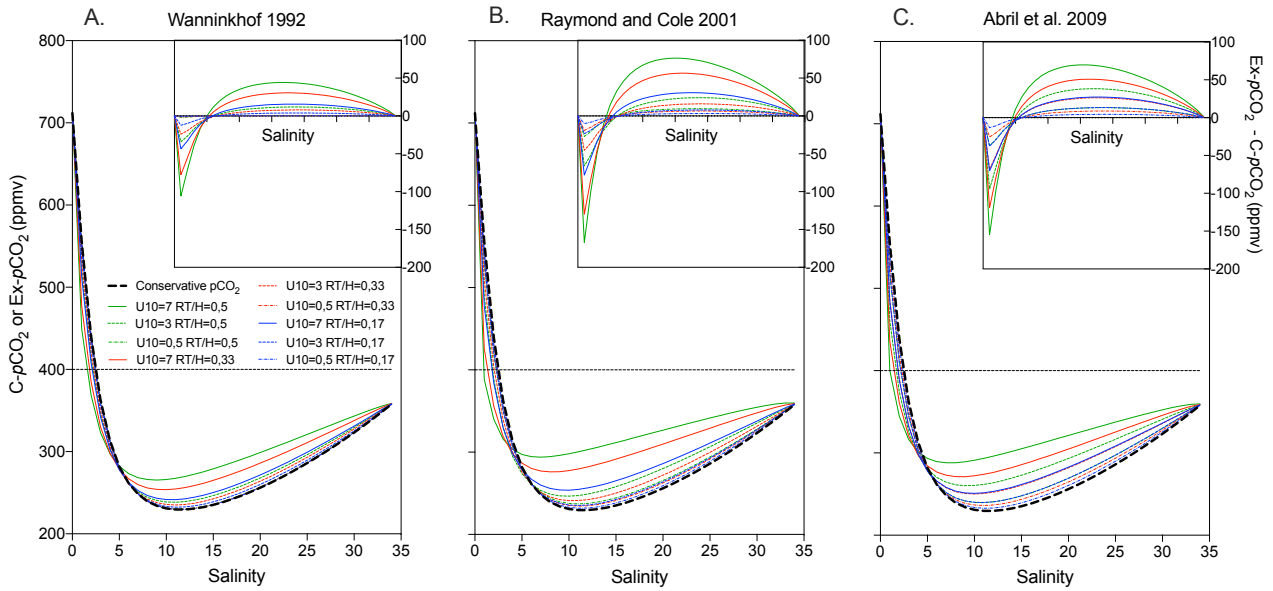
37 Figure 4. Time course of physico-chemical parameters in surface water of the main channel of the
 38 São Francisco River Estuary during the 25h cycle in Nov. 2015 (summer and spring tides). (A.)
 39 Temperature and Salinity and (B.) measured O- $p\text{CO}_2$ (black line), temperature-normalised T- $p\text{CO}_2$
 40 (red line), and the C- $p\text{CO}_2$ induced by conservative mixing of seawater with freshwater calculated
 41 from the salinity record (blue line). Upward blue arrows indicate the occurrence of tidal pumping,
 42 net heterotrophy and gas exchange (invasion of atmospheric CO_2). Upward red arrows indicate the
 43 impact of heating on $p\text{CO}_2$. Green double arrows indicate the significant diurnal change in low
 44 salinity waters.

45

46

47

48
49
50
51

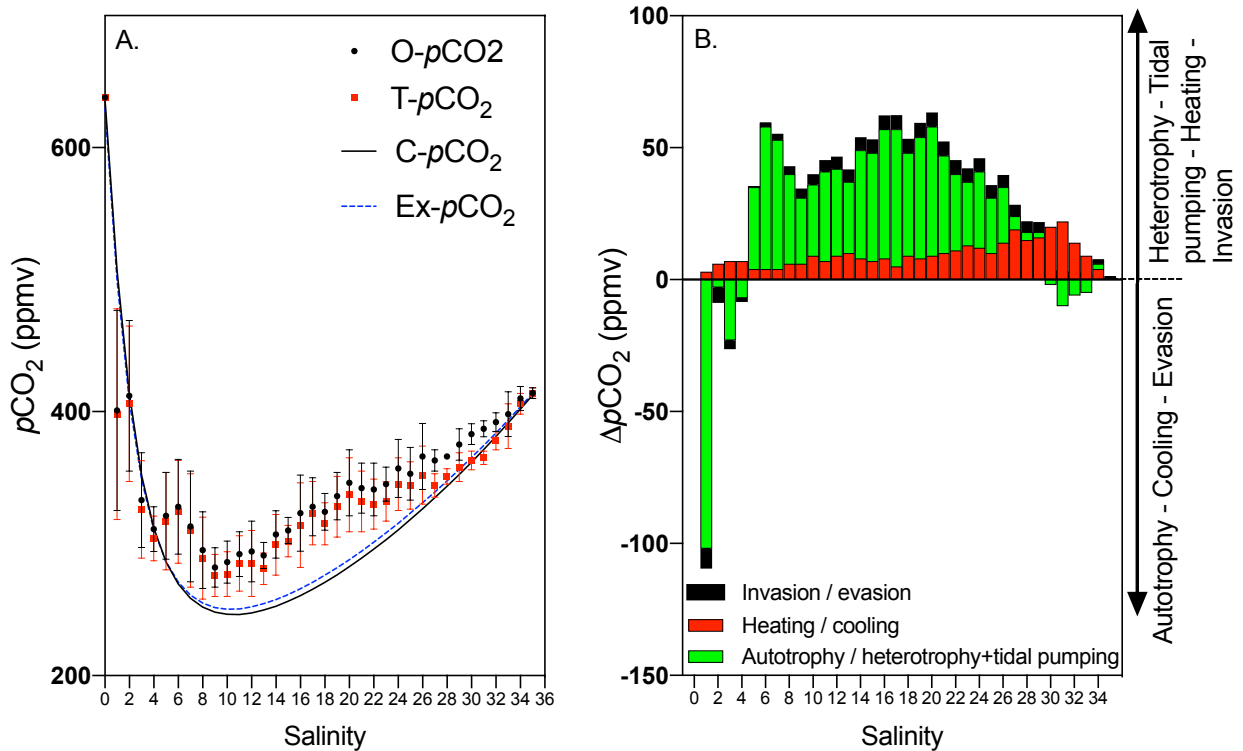


52

53 Figure 5. Impact of air-water CO₂ exchange on thermodynamic conservative $p\text{CO}_2$ mixing curves.
54 Calculations were made using Temperature, Salinity, DIC and TA observed in the freshwater and
55 marine end-members in Nov. 2015 and the gas exchange was computed every salinity unit
56 increment (see section 2.2). RT/H is the ratio between residence time and water depth, and the
57 selected value of 0,17 is representative for estuarine systems such as the São Francisco, whereas
58 the value may apply to larger tropical rivers such as the amazon or congo.

59

60



62

63 Figure 6. Comparison between measured and modelled $p\text{CO}_2$ along the salinity gradient of the
 64 São Francisco Estuary during the summer and spring tide cruise in Nov. 2015. A: measured O-
 65 $p\text{CO}_2$ binned for one salinity increments (blue dots with standard deviations as error bars), T- $p\text{CO}_2$
 66 normalized to a temperature corresponding to the conservative mixing of river and sea waters (red
 67 dots with standard deviations as error bars), modelled C- $p\text{CO}_2$ by considering the conservative
 68 mixing of TA, DIC and temperature in waters from the river and the sea (black full line), and
 69 modelled Ex- $p\text{CO}_2$ for conservative mixing corrected for gas exchange (blue dashed line). B:
 70 residual between the modelled and observed $p\text{CO}_2$. Invasion or evasion (black bars) is calculated
 71 as the difference between the C- $p\text{CO}_2$ and Ex- $p\text{CO}_2$ curves. Heating or cooling (red bars) is
 72 calculated as the difference between the O- $p\text{CO}_2$ and T- $p\text{CO}_2$. Autotrophy or heterotrophy and
 73 tidal pumping (green bars) is calculated as the residual, i.e. as the difference between the T- $p\text{CO}_2$
 74 Ex- $p\text{CO}_2$.

75

76

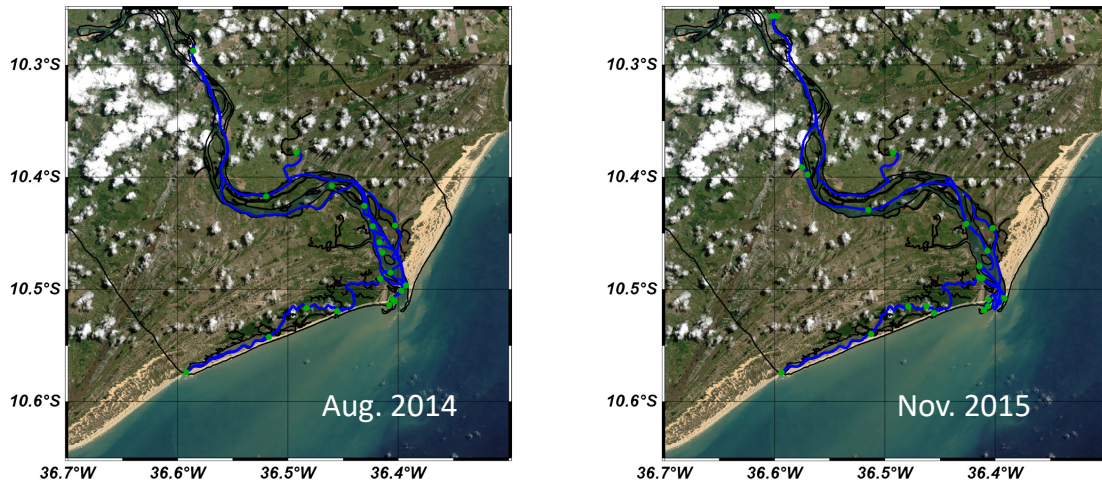
77

78 Supplementary Material

79

80 Figure S1.

81



82

83 Figure S1. Track of the boat (blue lines) and discrete sampling (green dots) during the two field

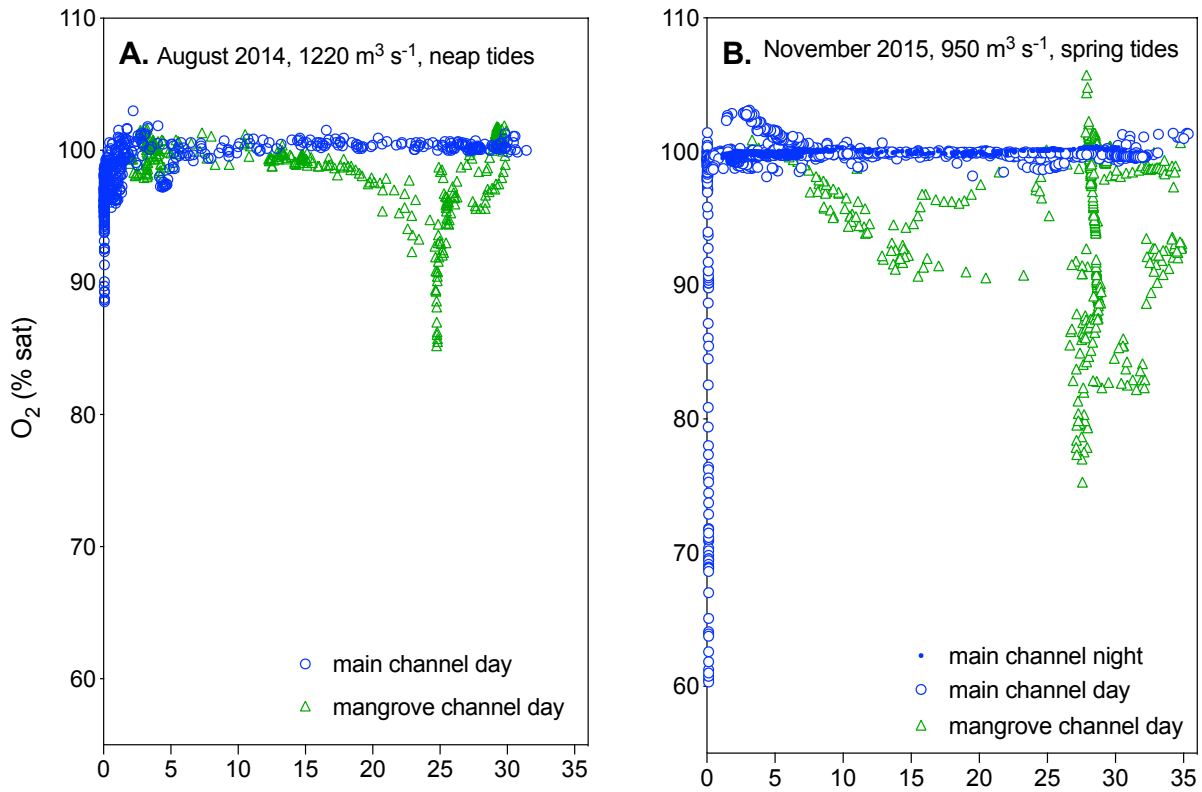
84 trips.

85

86 Figure S2

87

88



89

90 Figure S2. Distribution of dissolved oxygen (in percent of saturation) versus salinity in the São
91 Francisco Estuary main channel (blue circles) and mangrove secondary channel (green triangles)
92 in Aug. 2014 (A) and Nov. 2015 (B).

93

94